Analytical solutions for analysing pumping tests near an infinite vertical and anisotropic fault zone based upon unconventional application of well-image theory

Benoît Dewandel, Vivien Hakoun, Sandra Lanini, Claudine Lamotte, Jean-Christophe Maréchal

Analytical solutions for analysing pumping tests near an infinite vertical and anisotropic fault zone based upon unconventional application of well-image theory

Benoît Dewandel*[,1,2], Vivien Hakoun[1,2], Sandra Lanini[1,2], Bernard Ladouche[1,2], Claudine Lamotte[1] and Jean-Christophe Maréchal[1,2]

(1) BRGM, Univ Montpellier, Montpellier, France

(2) G-eau, UMR 183, INRAE, CIRAD, IRD, AgroParisTech, Supagro, BRGM, Montpellier, France

b.dewandel@brgm.fr; v.hakoun@brgm.fr; s.lanini@brgm.fr, b.ladouche@brgm.fr; c.lamotte@brgm.fr; jc.marechal@brgm.fr

* Corresponding author

Abstract

We present a new set of analytical solutions for analysing pumping tests in a well near a vertical fault zone, dyke or vein. We consider a fault zone with finite width, storativity and hydraulic conductivity, which can be anisotropic, and without limitation of the diffusivity contrast between the three aquifer domains (pumped aquifer, fault zone and opposite-side aquifer). This configuration, not described before, also considers flow transience within the fault zone. Drawdown solutions were developed for the three-aquifer domains based on an unconventional application of the well-image theory. Their comparison with numerical modelling results was very satisfactory. Drawdown behaviour at the pumping well is discussed for contrasted properties between the three-aquifer domains. Original analytical solutions for transient flow along both sides of the fault zone, and net transient flow from the fault itself, are proposed and discussed, with particular attention to flow reversal, from the pumped compartment to the fault zone, which occurs where the fault zone is the most transmissive. Finally, we extend the solutions to the case of a well intersecting and pumping a vertical fracture of finite length located near the same vertical geological discontinuity.

Keywords: Pumping test, Anisotropic fault, Pumping near a fault, Compartmented aquifer, Analytical solution

1. Introduction

In hydrogeology, the oil-and-gas industry, and geothermal activities, well testing is an essential tool for assessing the hydrodynamic properties of a reservoir. The evaluation of these properties, as well as their variability in space, is essential for improving resource management (e.g., Raghavan, 2004; Dewandel et al., 2012). In addition, detailed groundwater flow conditions, particularly in fractured systems, are required for pressure and transfer modelling, for instance in the case of a nuclear-waste deposit, geothermal exploitation, or contaminant transport. Therefore, the design of an adequate conceptual model based on well-test data prior to quantification of the hydrogeologic parameters has been a topic of interest for decades (Bourdet et al., 1983, 1989; Ehlig-Economides, 1988; Renard et al., 2009; Rafini and Larocque, 2012; Ferroud et al., 2019, etc.).

A common case encountered in the field is a well located near a fault (Fig. 1a) that may act as a barrier or a conduit, or a combination of both, to flow (e.g., Maslia and Prowell, 1990, Haneberg, 1995, Bense et al., 2003). In sedimentary rock, but not only, faults may be permeable, or act as low- or non-permeable structures, because the throw along the fault plane may be such that a permeable layer on one side of the fault is completely, or partially, juxtaposed against an impermeable layer on the other side, or because of low hydraulic conductivity materials in the core of the fault zone. The reverse is also possible, where the rock's hydraulic conductivity is enhanced because of unaltered fracturing along the fault zone (Caine et al., 1996). Other geological features, such as dykes, veins, or karst conduits, may locally enhance the hydraulic conductivity, and drain the surrounding aquifer, or act as a barrier or low-permeability discontinuity to flow (Dewandel et al., 2011, Perrin et al. 2011; Lachassagne et al., 2011, 2021, Maréchal et al. 2014; Xiong et al., 2017; Xu et al., 2018).

Depending upon the properties of the fault or of the geological discontinuity, fluid flow may occur along the structure and across the structure's planes. Several analytical studies have described transient pressure behaviour in the pumping well and flow processes; such work often refers to a pumping well near a fault of infinite length with finite-conductivity (Abbaszadeh and Cinco-Ley, 1995, Abbaszadeh et al., 2000; Escobar et al., 2013). Yaxley (1987) derived an analytical solution from Bixel's et al. (1963) work for a well located near a partially communicating vertical fault. This model, dedicated to low-permeable barrier, does not account for flow along the fault plane. Abbaszadeh and Cinco-Ley (1995) presented a

solution for a well located near a finite-conductivity vertical fault, with fracture skin for simulating damage zones on the sides of the fault plane. Their solution allowed varying aquifer properties on both sides of the fault, considered flow along and across the fault plane, but assumed a small fault width and neglected fault storativity and thus flow transience in the fault zone, the net flux in/out of the fault being nil. This model was dedicated to fault zones with higher hydraulic conductivity than those of the surrounding aquifers. Later, Rahman et al. (2003) proposed a semi-analytical solution similar to Abbaszadeh and Cinco-Ley (1995)'s work, to account for transient flow in the fracture plane, but also assumed a greater hydraulic conductivity in the fault. Other solutions exist in the literature, such as that developed by Boussila et al. (2003) for a well near a linear leaky boundary in laterally infinite composite systems, or the one proposed by Althawad (2016) for a pumping well intersecting and pumping a finite conductivity fracture of infinite length near a finite conductivity fracture of infinite length.

Vertical faults, or other vertical geological discontinuities, can also be conceptualized as vertically compartmented aquifers. Butler and Liu (1991) and Dewandel et al. (2014), proposed solutions for investigating the influence of a pumping well located in a linear strip aquifer—representing the geological discontinuity—bounded laterally by aquifers of differing properties. However, no analytical solution was provided for a pumping well located in one of the two external compartments and thus near the geological discontinuity. Anderson (2006), using the method of images, presented an analytical solution for a pumping well near such a discontinuity. His solution allows considering the anisotropy in hydraulic conductivity of the central compartment, the one representing a vertical fault zone, or another vertical geological discontinuity. However, this solution was established for steady-state flow only. Rafini and Larocque (2009) used numerical models for assessing the flow behaviour induced by a pumping test near a fault zone, embedded in a low-permeable matrix with various fault inclinations, but they did not consider the anisotropy in hydraulic conductivity of the fault zone.

We propose new analytical solutions for drawdown induced by a pumping well near an infinite sub-vertical and anisotropic fault zone (or another vertical geological discontinuity). We consider a fault zone of finite width, storativity and hydraulic conductivity that can be anisotropic (Fig. 1a), without limitation of the diffusivity contrast between the three-aquifer domains (pumped aquifer, fault zone and opposite-side aquifer), which was not considered in earlier works. Our solutions are based upon an unconventional application of the well-image

theory. Solutions are first developed for an isotropic fault and then extended to the anisotropic case; they are given for the three-aquifer domains and are compared to numerical modelling. The hydrodynamic signatures of drawdown and flow behaviour at the pumping well are discussed. Analytical solutions for transient flow along both sides of the central compartment (the fault zone) are given in terms of spatial and transient evolution, with particular attention to reversed flow, i.e. flow from the pumped compartment entering the fault zone, which can occur under specific conditions. These new solutions allow discussing the transient behaviour of such flow, which has not been studied in the past. Finally, we show that the solutions can be extended to other cases, such as a well intersecting and pumping a vertical fracture of finite length located near an infinite vertical fault zone (Fig. 1b).

The proposed solutions should be useful for examining and modelling drawdown created by a pumping well, or a well intersecting and pumping a vertical fracture, near a vertical fault zone, or another vertical geological discontinuity, such as dykes, veins, buried channels embedded in other materials, or even karst conduits.

2. Theoretical method and mathematical model

2.1. Conceptual model

The problem of interest consists in evaluating drawdown as a function of coordinates x, y and time, caused by a pumping well near an infinite vertical fault (or geological discontinuity) with finite thickness, finite storativity and anisotropic hydraulic conductivity (Fig. 1a). Following Anderson's (2006) nomenclature, the system is divided in three domains, D1, D* and D2, with L1 representing the boundary between D1 and D*, and L2 the one between D* and D2. Domain D*, the infinite vertical fault, separates two semi-infinite half-spaces. The pumping well is located in D1; it is at the origin of a Cartesian coordinate system (x=0, y=0) and is at a distance a from L1. The y-axis is parallel to the two boundaries L1 and L2. The well fully penetrates the aquifer and produces at a constant flowrate Q. The overall domain (D1, D*, D2) assumes a confined condition; each domain is characterized by its own transmissivity and storativity. D* has anisotropic hydraulic conductivity in the horizontal plane, while the two other domains are isotropic. Domain thicknesses can be different (not shown on Fig. 1a). Damage zones along the fault zones (D*) are not considered.

2.2. Method of images

The method of images is a classic technique for tackling boundary-value problems, such as those encountered in heat conduction, electrostatics, and, particularly, in groundwater flow, to solve the problem of no-flow, constant boundaries, or leaky boundaries (Ferris et al., 1962; Kruseman et al., 1990; Bruggeman, 1999; Anderson, 2000, 2006). Solutions with this method have the advantage of providing convenient forms, compared to solutions from differential equations that may require numerical inversion of a Laplace transform. The proposed solutions are based upon an unconventional application of the well-image theory. This method, originally proposed by Fenske (1984) for the case of a boundary separating two aquifers with dissimilar diffusivities, and later extended by Dewandel et al. (2014) to a well located in an infinite linear strip aquifer limited on both sides by aquifers of differing properties, has been further developed for the case presented here. Though good and useful approximations, the proposed solutions are not shown to be exact solutions to the appropriate partial differential equations (Bixel et al., 1963; Butler and Liu, 1991; Appendix A, hereafter). We do believe, however, that—although it is not the method used here—drawdown solutions can also be obtained by numerical inversion of a Laplace transform.

In a general manner and using the well-image theory for the case presented here, one can consider the drawdown in domain D1 to consist of two components: direct drawdown caused by the pumping well, and reflected drawdowns caused by the reflection of image-well drawdowns from the two boundaries onto D1. Total drawdown can be represented by a sum of drawdowns caused by the pumping well and that caused by image-wells located across the boundaries; each image-well is strengthened to consider the contrast in properties between the three domains. Figure 2a shows the solution for drawdown in D1, where each dot corresponds to an image well with its distance from the pumping well and its strength. This technique is widely used for solving the particular cases of no-flow and constant-head boundary conditions (e.g. Ferris et al., 1962; Kruseman et al., 1990); in these cases, image strength is 1 or -1. More information on the well-image theory can be found in Anderson (2000, 2006), or in Bruggeman (1999).

The drawdown in domains D* and D2 is the transmitted drawdown across the boundaries. Its solutions depend upon the properties of the domain of interest and are analogues of the solution in D1. Consequently, drawdown can also be represented as the sum of drawdowns caused by the producing well, and one or two infinite well-image series—depending upon the

domain—lying outside the domain of interest, whereby each pumping- and image well was strengthened to cover the aquifer properties of each domain (Figs. 2b and 2c).

Along the boundaries, conditions vary from boundary L1 (between D1 and D*) to boundary L2 (between D* and D2) and the following criteria must be satisfied:

1). Drawdown must be equal on both sides of the boundaries:

- then $s_1(a,y,t) = s^*(a,y,t)$ along boundary L1,

- and $s_2(a+h,y,t) = s^*(a+h,y,t)$ along boundary L2,

2). Unit discharge orthogonal to the boundaries must be equal on both sides as well:

- then $T_1 \frac{\partial s_1(a,y,t)}{\partial x} = T^* \frac{\partial s^*(a,y,t)}{\partial x}$ along boundary L1,

- and $T_2 \frac{\partial s_2(a+h,y,t)}{\partial x} = T^* \frac{\partial s^*(a+h,y,t)}{\partial x}$ along boundary L2,

where $s_1(x,y,t)$, $s^*(x,y,t)$ and $s_2(x,y,t)$ are the drawdowns in each domain (D1, D* and D2), T_1, T^* and T_2 are the transmissivity values of each domain, a is the distance from the pumping well to boundary L1, and h is the width of domain D*.

2.3. General solutions for drawdown

Here, we first considered the case where domain D* is isotropic. A second section deals with the anisotropy of this domain. All three domains are characterized by dissimilar diffusivity values ($T_1/S_1 \neq T^*/S^* \neq T_2/S_2$).

Using the well-image theory described above, the general solutions for drawdown valid for each domain are expressed as series (Fig. 2). For domain 1 (D1), drawdown is expressed by that of the producing well, that of one image-well at the opposite of L1 (at $x=2a$), and that of one infinite image-well series lying outside D1. For domain D*, drawdown is expressed by two infinite image-well series lying outside D*, and for D2 by one infinite image-well series lying outside D2.

The general form of solutions for drawdown are as follows, for an observation well in domain D1:

$$s_1(x,y,t) = \frac{Q}{4\pi T_1}\left\{ \mathrm{W}\left(\frac{S_1}{4T_1 t}(x^2+y^2)\right) + \alpha_0 \mathrm{W}\left(\frac{S_1}{4T_1 t}([2a-x]^2+y^2)\right) + \sum_{n=2,4,6}^{\infty} \alpha_i \mathrm{W}\left(\frac{S_1}{4T_1 t}([2a+nh-x]^2+y^2)\right)\right\} \quad (1)$$

For domain D*:

$$s^*(x,y,t) = \frac{Q}{4\pi T^*}\left\{ \sum_{n=2,4,6}^{\infty} \beta_i' \mathrm{W}\left(\frac{s^*}{4T^* t}([2a+nh-x]^2+y^2)\right) + \sum_{n=0,2,4}^{\infty} \beta_i \mathrm{W}\left(\frac{s^*}{4T^* t}([2nh+x]^2+y^2)\right)\right\} \quad (2)$$

And for domain D2:

$$s_2(x,y,t) = \frac{Q}{4\pi T_2}\left\{ \sum_{n=0,2,4}^{\infty} \delta_i \mathrm{W}\left(\frac{S_2}{4T_2 t}([2nh+x]^2+y^2)\right)\right\} \quad (3)$$

where W(u) is the well-function (or exponential integral function also noted -Ei [-u]); S_1 and T_1 (m^2/s) are the storage coefficient and transmissivity of the aquifer in D1, respectively; S* and T* (m^2/s) are those of the strip aquifer in D*, and S_2 and T_2 (m^2/s) those of aquifer D2; a (m) is the distance from the pumping well to L1; and Q is the pumping rate (m^{3}s^{-1}); α_0, α_n, β_i', β_i and δ_i are the image-well strengths. Now, we must evaluate the strength coefficients of each image-well.

2.4. Drawdown solutions for the three domains

2.4.1. Isotropic case

We consider the first series of images according to L1 and L2 (Fig. 3a). The pumping well is first imaged according to L1. The result of applying the two boundary conditions at boundary

L1 ($s_1(a,y,t) = s^*(a,y,t)$ and $T_1 \frac{\partial s_1(a,y,t)}{\partial x} = T^* \frac{\partial s^*(a,y,t)}{\partial x}$) is that the two strength coefficients α_0 and β_0 depend upon the contrast of diffusivity between domains D1 and D*, the distance to the boundary (a) and time (t). Appendix B gives the detail of their solutions. This case refers to the influence of a partial hydrologic barrier that separates two domains with contrasted diffusivities, where the drawdown solutions for both domains D1 and D* correspond to the ones proposed by Fenske (1984). Then, considering the case of two parallel boundaries L1 and L2, and thus that of a well pumping near an infinite strip aquifer, the pumping well must be imaged about the second boundary L2 (2nd image), which allows evaluating strength coefficients β_0' and δ_0 (Fig. 3a), while applying the new boundary conditions ($s_2(a+h,y,t) = s^*(a+h,y,t)$ and $T_2 \frac{\partial s_2(a+h,y,t)}{\partial x} = T^* \frac{\partial s^*(a+h,y,t)}{\partial x}$).

These strengths depend upon previous ones β_0 for β_0', but also on the diffusivity contrast between domains D* and D2, on the width of domain D* (h), and on time (t); Appendix B gives the detail of their solutions. Then, as this last image-well does not respect the conditions at boundary L1, it must be imaged about L1 (3rd image), which allows evaluating strength coefficients α_1 and β_1 according to boundary conditions in L1 (Fig. 3b). As the 3rd image does not respect the condition along L2, it has to be imaged about L2 (4th image) and strength coefficients β_1' and δ_1 should be evaluated according to boundary conditions in L2 (Fig. 3b), and so on. Therefore, each iteration results in a new image-well with a strength evaluated according to boundary conditions at L1 and L2. As the strength of the nth image-well depends upon the product of all previous image-strengths, the strengths of each image-well series can be expressed as a combination of arithmetic and geometrical series. The drawdown for an observation well located in D1 is:

$$s_1(x,y,t) = \frac{Q}{4\pi T_1}\left\{ \mathrm{W}\left(\frac{S_1}{4T_1 t}(x^2+y^2)\right) + \frac{T_1\tau_0 - T^*\gamma_0}{T_1\tau_0 + T^*\gamma_0}\mathrm{W}\left(\frac{S_1}{4T_1 t}([2a-x]^2+y^2)\right) + \frac{2T^*\gamma_0\tau_0}{T_1\tau_0 + T^*\gamma_0}\sum_{n=2,4,6}^{\infty} \frac{2T_1}{T_1\tau_n + T^*\gamma_n}\prod_{i=1,3,5}^{n-1}\frac{T^*\tau_i - T_2\gamma_i}{T^*\tau_i + T_2\gamma_i}\prod_{i=2,4,6}^{n-2}\frac{T^*\gamma_i' - T_1\tau_i'}{T^*\gamma_i' + T_1\tau_i'} \mathrm{W}\left(\frac{S_1}{4T_1 t}([2a+nh-x]^2+y^2)\right) \right\} \quad (4)$$

with the second geometrical series (the one up to '*n*-2') valid for *n*>2.

For a well located in D*, the drawdown is:

$$s^*(x,y,t) = \frac{Q}{4\pi T^*}\left(\frac{2T^*\gamma_0\tau_0}{T_1\tau_0 + T^*\gamma_0}\right)\left\{\sum_{n=2,4,6}^{\infty}\prod_{i=1,3,5}^{n-1}\frac{T^*\tau_i - T_2\gamma_i}{T^*\tau_i + T_2\gamma_i}\prod_{i=2,4,6}^{n-2}\frac{T^*\gamma_i' - T_1\tau_i'}{T^*\gamma_i' + T_1\tau_i'}\right.$$
$$\left.\mathrm{W}\left(\frac{s^*}{4T^*t}([2a+nh-x]^2+y^2)\right) + \sum_{n=0,2,4}^{\infty}\prod_{i=1,3,5}^{n-1}\frac{T^*\tau_i - T_2\gamma_i}{T^*\tau_i + T_2\gamma_i}\prod_{i=2,4,6}^{n}\frac{T^*\gamma_i' - T_1\tau_i'}{T^*\gamma_i' + T_1\tau_i'}\mathrm{W}\left(\frac{s^*}{4T^*t}([nh+x]^2+y^2)\right)\right\} \quad (5)$$

with the second geometrical series of the first arithmetic series (the one up to '*n*-2') valid for *n*>2, and both geometrical series of the second arithmetic series (the ones up to '*n*-1' and '*n*') valid for *n*>1.

For a well located in D2, the drawdown is:

$$s_2(x,y,t) = \frac{Q}{4\pi T_2}\left(\frac{2T^*\gamma_0\tau_0}{T_1\tau_0 + T^*\gamma_0}\right)\left\{\sum_{n=0,2,4}^{\infty}\frac{2T_2\gamma_{n+1}\tau_{n+1}}{T_2\tau_{n+1} + T^*\gamma_{n+1}}\prod_{i=1,3,5}^{n-1}\frac{T^*\tau_i - T_2\gamma_i}{T^*\tau_i + T_2\gamma_i}\prod_{i=2,4,6}^{n}\frac{T^*\gamma_i' - T_1\tau_i'}{T^*\gamma_i' + T_1\tau_i'}\right.$$
$$\left.\mathrm{W}\left(\frac{S_2}{4T_2t}([nh+x]^2+y^2)\right)\right\} \quad (6)$$

with both geometrical series (the ones up to '*n*-1' and '*n*') valid for *n*>1.

$$\text{with : } \gamma_0 = \frac{\mathrm{W}\left(\frac{S_1}{4T_1t}(a^2+y^2)\right)}{\mathrm{W}\left(\frac{s^*}{4T^*t}(a^2+y^2)\right)}\ ;\ \tau_0 = \frac{\mathrm{e}\left(-\frac{S_1}{4T_1t}(a^2+y^2)\right)}{\mathrm{e}\left(-\frac{s^*}{4T^*t}(a^2+y^2)\right)}$$

$$\gamma_i = \frac{\mathrm{W}\left(\frac{s^*}{4T^*t}([a+ih]^2+y^2)\right)}{\mathrm{W}\left(\frac{S_2}{4T_2t}([a+ih]^2+y^2)\right)}\ ;\ \tau_i = \frac{\mathrm{e}\left(-\frac{s^*}{4T^*t}([a+ih]^2+y^2)\right)}{\mathrm{e}\left(-\frac{S_2}{4T_2t}([a+ih]^2+y^2)\right)}$$

$$\gamma_i' = \frac{\mathrm{W}\left(\frac{S_1}{4T_1t}([a+ih]^2+y^2)\right)}{\mathrm{W}\left(\frac{s^*}{4T^*t}([a+ih]^2+y^2)\right)}\ ;\ \tau_i' = \frac{\mathrm{e}\left(-\frac{S_1}{4T_1t}([a+ih]^2+y^2)\right)}{\mathrm{e}\left(-\frac{s^*}{4T^*t}([a+ih]^2+y^2)\right)}$$

$$\gamma_n = \frac{\mathrm{W}\left(\frac{S_1}{4T_1t}([a+nh]^2+y^2)\right)}{\mathrm{W}\left(\frac{s^*}{4T^*t}([a+nh]^2+y^2)\right)}\ ;\ \tau_n = \frac{\mathrm{e}\left(-\frac{S_1}{4T_1t}([a+nh]^2+y^2)\right)}{\mathrm{e}\left(-\frac{s^*}{4T^*t}([a+nh]^2+y^2)\right)}$$

238 $$\gamma_{n+1} = \frac{\mathrm{W}\left(\frac{s^*}{4T^*t}([a+(n+1)h]^2+y^2)\right)}{\mathrm{W}\left(\frac{S_2}{4T_2t}([a+(n+1)h]^2+y^2)\right)} \; ; \; \tau_{n+1} = \frac{\mathrm{e}\left(-\frac{s^*}{4T^*t}([a+(n+1)h]^2+y^2)\right)}{\mathrm{e}\left(-\frac{S_2}{4T_2t}([a+(n+1)h]^2+y^2)\right)}$$

239 where W(u) is the exponential integral and e(u) is the exponential function.

240 As a result, the strength coefficients depend upon geometrical series that are a function of
241 each domain diffusivity, time, the distance *a* from the pumping well to the first boundary
242 (L1), and the width *h* of the strip aquifer (width of D*). In each infinite series, the strength
243 coefficient of each image well decreases with distance from both boundaries, and each series
244 converges absolutely. To solve Eqs. 4 to 6, we used an algorithm based on an iterative
245 process, where the number of images is determined when the absolute value of a certain
246 metric given by the nth computation (of the nth becomes negligible (e.g. 10^{-6}). This criterion
247 ensures high computation accuracy.

248 Note that for the case of time-constant strength coefficients (equal-diffusivity ratio between
249 the compartments), the solutions are the same as those of the appropriate partial differential
250 equation. Solutions of this particular case are given in Appendix (C) for the three-aquifer
251 domains, and, as expected, strength coefficients are identical to the ones given in Anderson
252 (2006), for a solution in steady-state condition.

253

254 *2.4.2. Anisotropic case*

255 Analytical solutions for the three domains can be obtained for the case where the geologic
256 discontinuity (D*) has an anisotropic transmissivity (or hydraulic conductivity). These
257 solutions are based on the isotropic solutions (Eqs. 4 to 6) and standard transformed
258 coordinate techniques (e.g., Hantush, 1966; Ramey, 1975; Neuman et al., 1984). It is assumed
259 that the main axes of transmissivity in D* are oriented along the *x*- and *y*-directions, thus T_y^*
260 and T_x^* are parallel and orthogonal to both boundaries, respectively, and $T^* = \sqrt{T_x^* T_y^*}$. As the
261 pumping well fully penetrates the aquifer (in D1), flow lines are parallel to the bottom of the
262 aquifer. Consequently, the anisotropy of hydraulic conductivity in the vertical plane is not
263 considered.

264 According to Bear and Dagan (1965) and Anderson (2006), the transformed coordinates in D1
265 remain unchanged. However, in D2, *x* coordinate must be shifted to the right along the *x*-axis
266 to account for the transformed width of D*, i.e. $h\sqrt{\frac{T_y^*}{T_x^*}}$. Therefore:

in D1, $\dot{x} = x$ and $\dot{y} = y$ (7)

and in D2, $\ddot{x} = x + h\left(\sqrt{\frac{T_y^*}{T_x^*}} - 1\right)$ and $\ddot{y} = y$ (8)

In D*, the transformed coordinates are more complex because of rotational flow in D*. They are $\ddot{x} = x'\sqrt{\frac{T_y^*}{T_x^*}}$ and $\ddot{y} = y$, where x' is a function of the real-coordinate system that assumes at boundary L1 (i.e. between D1 and D*): $\dot{x} = \ddot{x} = x' = a$, and at the second boundary L2 (i.e. between D* and D2): $\ddot{x} = \ddot{x} = x' = a + h\sqrt{\frac{T_y^*}{T_x^*}}$). These re-scaling relationships show that D* must also be shifted to the right along the *x*-axis to account for the transformed width $h\sqrt{\frac{T_y^*}{T_x^*}}$. According to Dewandel et al. (2014), x' can be estimated empirically; it is found that $x' = x + a\left(\sqrt{\frac{T_x^*}{T_y^*}} - 1\right)$, which gives for $a \leq x \leq a+h$:

$$\ddot{x} = \sqrt{\frac{T_y^*}{T_x^*}}(x - a) + a \quad (9)$$

The evaluated relationship still depends on the anisotropy ratio in D* and is linear, which agrees with Baer and Dagan (1965).

Drawdown solutions in the transform domains are not re-written as they use isotropic solutions (Eqs. 4, 5, 6), where h is replaced by $h\sqrt{\frac{T_y^*}{T_x^*}}$ and T^* by $\sqrt{T_x^* T_y^*}$. In Eq. 5 (for an observation well in D*) x is replaced by $\ddot{x}$, and in Eq. 6 (for a well in D2) x is replaced by $\ddot{x}$, according to the previous re-scaling rules (Eqs. 9 and 10). The y coordinates remain unchanged, as well as the x coordinates in Eq. 4 (for a well in domain D1). Re-scaling of all three domains also satisfies long pumping stages, when drawdown solutions are characterized by straight lines on semi-log plots whose slope values depend on the average transmissivity of domains D1 and D2. These solutions are compared with numerical modelling, particularly the one in D*, in Section 4. *Comparisons between the developed solutions and numerical simulations*).

3. Drawdown and flow behaviour at the pumping well

3.1. Isotropic case

As many type curves exist for describing flow behaviour near such a discontinuity (domain D*), some examples are given below to discuss the main flow behaviour characteristics.

Figure 4 shows the result of Eq. 4 at a pumping well of radius r_w ($x_w = y_w = \sqrt{2}r_w$) using dimensionless time, $t_{DL} = T_1 t/(S_1 a^2)$, and dimensionless drawdown, $s_D\left({}^{r_w}/_{a}, t_{DL}\right) = \frac{2\pi T_1}{Q} s_{pw}(r_w, t)$, for the case where T_1/S_1=0.1, T_2/S_2=0.5, T_1/T_2=20.0, h= 5 m. Figure 4a presents the case where T^*/T_1 varies from 10^{-2} to 10^3 with S^*/S_1 =20.0, and Figure 4b the case where S^*/S_1 varies from 10^{-3} to 10^3 with T^*/T_1=100.0. Diffusivity in D* thus varies between 10^{-2} and 10^3. The dimensionless forms of the solutions (Eqs. 4 to 6) are provided as Supporting Information.

A convenient starting point for the analysis of Eq. 4 is the log-log diagnostic plot developed by Bourdet et al. (1983). In this plot, both drawdown (s_D) and its derivative (s_D') are shown with respect to the natural logarithm of time ($\partial s_D/\partial Ln(t_{DL})$). Among others, this log-log plot is commonly used for identifying flow regimes during a pumping test (Ehlig-Economides, 1988; Bourdet et al., 1989; Spane and Wurstner, 1993; Renard et al., 2009; Ferroud et al, 2019). For all presented derivative curves in this work, derivatives were computed numerically according to Bourdet's et al. (1989) algorithm.

During the early stages of pumping, when the cone of depression has not yet reached boundary L1 (t_{DL}<0.2 on Figs. 4a and b), Eq. 4 is identical to the solution of an infinite homogeneous aquifer (Theis, 1935). For a large enough t_{DL}, the condition for which Theis' equation reduces to Cooper-Jacob's (1946) equation, a straight line on a semi-logarithmic plot with a slope ½ characterizes dimensionless drawdown. Its logarithmic derivative is constant (value of ½), reflecting the first infinite-radial flow to the well (Fig. 4). Therefore, for short times, the logarithmic derivative of drawdown will converge to $\partial s/\partial Ln(t) = Q/4\pi T_1$.

Once the cone of depression begins to reach boundary L1 (t_{DL}>0.2), transmissivity and storage-coefficient ratios between the pumped (D1) and the strip (D*) aquifers change the character of the drawdown curves. At that time, the drawdown propagates along boundary L1 and within the strip aquifer. For high T^*/T_1 or S^*/S_1 ratios, the derivative slope tends to -1, showing that the fault zone acts as a steady-state source (i.e. constant head boundary; Abbaszadeh and Cinco-Ley, 1995, Abbaszadeh et al., 2000). The higher the T^*/T_1 or S^*/S_1 ratios, the more the -1 slope is established and the longer it lasts. Note that this trend generally characterizes a fault zone with infinite hydraulic conductivity near a pumping well

(Abbaszadeh and Cinco-Ley, 1995, Abbaszadeh et al., 2000; Escobar et al., 2013). However, Fig. 4b also shows that a similar trend can be obtained for high S^*/S_1 ratios and not necessarily high T^*/T_1 ratios, as in the previously cited literature. Then, at medium-stages (t_{DL}>10.0), when the fault begins to drain the whole aquifer system, derivatives follow a near ¼ slope, which describes a bi-linear flow regime within D*, as mentioned in previously cited work. However, when S^*/S_1 ratios are high (>100.0 on Fig. 4b) the derivative's slope tends to ½, describing a linear flow regime within D*. It is also interesting to note that, for intermediate T^*/T_1 ratios (with $T^*>T_1$) or S^*/S_1 ratios, drawdown behaves similarly to naturally fractured media like dual-porosity aquifers (Abbaszadeh and Cinco-Ley, 1995), or dual-permeability media such as multilayer aquifers.

When T^*/T_1 and S^*/S_1 ratios decrease (Figs. 4a and b), derivative curves rise up, and durations of the -1 derivative slope period and subsequent ¼ or ½ slope decrease (linear flow regimes), showing that D* is less able to drain the whole aquifer system. In the proposed examples, the derivative may form a hump at the end of the linear flow period within D* (t_{DL}>30 on Fig. 4a or 6 000 on Fig. 4b). On Fig. 4a, it is the consequence of a decrease in the T^*/T_1 ratio (<1), and on Fig. 4b it is the result of a lower diffusivity contrast between domains D* and D2. The smaller the contrast, the greater the hump, which may cause boundary L1 (Fig. 4a) and L2 (Fig. 4b) to appear temporarily as a no-flow boundary (see blue curves on Fig. 4a).

At late pumping stages (t_{DL}>10^5 on Figs. 4a and 4b), drawdown has diffused through the whole domain D* and propagates significantly in the third domain (D2). This period is characterized by a second radial flow regime, illustrating the overall response of the aquifer system.

During very late stages of pumping (i.e. $t\rightarrow\infty$ or $t_{DL}\rightarrow\infty$), all strength coefficients γ_i and τ_i in Eq.4, but also in Eqs. 5 and 6, tend to 1. Therefore, and after rearranging Eq. 4, the logarithmic derivative of the dimensionless drawdown for late-pumping stages leads to:

$$\mathrm{Lim}_{t_{DL}\rightarrow\infty}\frac{\partial s_D}{\partial t_{DL}} \approx \left(\frac{2T_1}{T_1+T^*}\right)\left\{1+\left(\frac{2T^*}{T_1+T^*}\right)\left(\frac{T^*-T_2}{T_2+T^*}\right)\sum_{n=0,1,2}^{\infty}\left(\frac{T^*-T_2}{T_2+T^*}\right)^n\left(\frac{T^*-T_1}{T_1+T^*}\right)^n\right\} \quad (10)$$

As $\left(\frac{T^*-T_2}{T_2+T^*}\right)$ and $\left(\frac{T^*-T_1}{T_1+T^*}\right)$ ratios are between -1 and 1, the series can be regarded as a Taylor series that tends, for $n\rightarrow\infty$, to $\frac{(T_1+T^*)(T_2+T^*)}{2T^*(T_1+T_2)}$. Therefore, the last equation simplifies to

$\mathrm{Lim}_{t_{DL}\to\infty} \frac{\partial s_D}{\partial t_{DL}} \approx \left(\frac{2T_1}{T_1+T_2}\right)$, showing that the logarithmic derivative of the dimensionless drawdown depends only on the transmissivities of the pumped aquifer (D1) and of domain D2. Thus, the logarithmic derivative of drawdown, $\partial s/\partial Ln(t)$, will converge to a constant value inversely proportional to the average transmissivities of D1 and D2, $\frac{\partial s}{\partial Ln(t)} = Q/[2\pi(T_1+T_2)]$. This shows that, for late-stage pumping, the drawdown slope does not depend on the transmissivity of the strip aquifer (D*, representing a fault, another geological discontinuity, or another compartment), but on those of the pumped compartment and of the compartment on the other side of the geological discontinuity. This behaviour agrees with previous work (Abbaszadeh and Cinco-Ley, 1995, Abbaszadeh et al., 2000; Rahman et al., 2003; Escobar et al., 2013).

3.2. Anisotropic case

As discussed above, the solution with an anisotropic central compartment (D*) is similar to that for the isotropic case (Eq. 4, h being replaced by $h\sqrt{\frac{T_y^*}{T_x^*}}$ and T^* by $\sqrt{T_x^* T_y^*}$). Therefore, drawdown and derivative curves are characterized by a similar behaviour (Fig. 5). During the early-stage pumping (t_{DL}<0.2), $\partial s_D/\partial Ln(t_{DL}) = 1/2$ (or $\partial s/\partial Ln(t) = Q/4\pi T_1$)—or the first infinite-acting radial flow when boundary L1 has not been reached by the pumping—and for late-stage pumping, $\partial s_D/\partial Ln(t_{DL})$ always tends to $\frac{2T_1}{T_1+T_2}$ (or $\frac{\partial s}{\partial Ln(t)} = Q/[2\pi(T_1+T_2)]$), which characterizes the overall response of the aquifer system. However, compared to the isotropic case ($T_x^*=T_y^*$, curves T^*/T_1=100.0 on Fig. 4a or S^*/S_1=20.0 on Fig. 4b), the T_y^*/T_x^* ratio increase induces a decrease of the derivative slope, up to -1 for the highest ratios (T_y^*/T_x^*>100.0), because of the increasing transmissivity contrast (T_y^*/T_1) in a direction perpendicular to the central compartment (x-axis). This shows that the anisotropy increase of transmissivity in D*, increases the capacity of the central compartment to drain the entire system, and thus its capacity to supply water to the pumped D1 compartment. Consequently, at medium-stage bi-linear flow (¼ derivatives slope) or linear flow (½ derivatives slope), regimes are shifted in time. The higher the T_y^*/T_x^* ratio, the greater the offset.

Conversely, a decrease in the anisotropy ratio (T_y^*/T_x^*<1.0, Fig. 5) induces a lower transmissivity contrast between D1 and D* (T_y^*/T_1). This reduces both the exchange between domains and the capacity of D* to drain the whole system. For the lowest contrast

383 ($T_y^*/T_x^*<10^{-2}$), D* may act as a semi-permeable boundary, even though the overall
384 transmissivity value of D* is still significantly higher than that of D1 (T^*/T_1=100.0, Fig. 5).

385

386 **4. Comparison between developed solutions and numerical simulations**

387 We compared the performance of solutions with transmissivity anisotropy in D* with
388 numerical modelling, to check their accuracy but also to evaluate Eq. 9 required for the
389 drawdown solutions in D*. The numerical modelling was developed with the MARTHE_7.4
390 ©BRGM computer code (Thiéry, 2010, 2015, 2018). MARTHE allows 2D or 3D modelling
391 of flow and mass transfers in aquifer systems, including climatic and human influences.
392 Groundwater flow is computed by a 3-D finite volume approach, to solve the hydrodynamic
393 equation based on Darcy's law and mass conservation. The grid geometry used in the
394 numerical model is a 40x40 km square grid with a constant-head boundary condition at each
395 side. In the *x*, *y* plane, cell size varies from 1x1 m at the origin (pumping well) up to
396 500x500 m near the limits of the model. Vertically, the pumped aquifer is a 100-m-thick layer
397 subdivided into 25 4-m-thick layers. The aquifer is capped by an impermeable layer (no-flow
398 condition), creating a confined condition for the pumped layer.

399 Several diffusivity ratios between the three domains and widths of the strip aquifer were
400 prescribed to test the isotropic and the anisotropic solutions at various observation-well
401 locations, i.e. in the pumped compartment D1, the strip aquifer D*, and in the right-side
402 compartment D2. Figure 6 shows the results of two of these models for testing the anisotropic
403 solutions. In the model, the pumping well fully penetrates the aquifer and is located at the
404 centre of the grid (x=0; y=0) and at 12 m (a=12 m) from a 8-m-wide strip aquifer (h=8 m). In
405 both cases, transmissivity in the pumped compartment D1, T_1, is 10^{-2} m^2/s (hydraulic
406 conductivity k_1=10^{-4} m/s), the storage coefficient S_1 is 2.0x10^{-2} (specific storage Ss_1=2x10^{-4} m^{-1}) and the transmissivity and storage coefficient of the right-hand side compartment (D2), T_2, is 5x10^{-3} m^2/s (k_2=5x10^{-5} m/s) and S_2 is 10^{-3} (Ss_2=10^{-5} m^{-1}), respectively. Only the properties of the strip aquifer (D*) differ, although the T^*_y/T^*_x anisotropy ratio is the same at 10.0. In Model 1, T^* is 10^{-1} m^2/s (k^*=10^{-3} m/s) and S^* is 10^{-1} (Ss^*=10^{-3} m^{-1}), and in Model 2, T^* is 3x10^{-3} m^2/s (k^*=3x10^{-5} m/s) and S^* is 2x10^{-2} (Ss^*=2x10^{-4} m^{-1}). Thus, in Model 1 the strip aquifer is the most transmissive and capacitive of the whole domain, while it is the least transmissive and the least capacitive in Model 2. For the simulations, a constant pumping rate

of Q=1.11x10^{-2} m^3/s (40 m^3/h) was set up for up to 700 days (about 10^6 min). In this context, the model's boundaries were not reached, and the aquifer remained saturated.

Figures 6a and b compare the results of numerical modelling with analytically computed drawdown values. As shown on the figures, drawdown values and derivatives computed with the proposed solutions (Eqs. 4 to 6 with the proposed re-scaling rules of Eqs. 7 to 9), for observation wells in the pumped aquifer (D1; curves A to D on figures), for the ones in the strip aquifer (D*; curves E and F) and for the ones in the right-side aquifer (D2; curves G and H), perfectly match the values from numerical modelling. The root mean square error (RMSE) was calculated for each numerical-analytical comparison of drawdown values (see inserted tables on Figures 6a and 6b). RMSE values range between 1.4x10^{-3} and 1.7x10^{-2} m, showing that the proposed analytical solutions agree with the numerical modelling, a good indication of their accuracy.

5. Flow along and through boundaries L1 and L2

As mentioned in earlier studies, flow through and across a fracture plane or geological discontinuity (domain D*) is complex, and may be locally reversed (Fig. 7), particularly where the fault-transmissivity is higher than that of other compartments (Abbaszadeh and Cinco-Ley, 1995, Abbaszadeh et al., 2000; Rahman et al., 2003). The aim of this section is to propose analytical solutions of such flows, and to highlight their spatial and transient evolutions under different diffusivity contrasts ($T_1/S_1 \neq T^*/S^* \neq T_2/S_2$). The dimensionless forms of the following solutions are provided as Supporting Information.

5.1. Analytical solutions for flows through L1 and L2

Analytical solutions for flow through both boundaries can be derived from Eqs. 4 to 6 for an isotropic central compartment (D*), and with re-scaling rules presented in section 2.4.2. for the anisotropic case (Eqs. 7 to 9).

The solutions for flow are normalized with respect to the pumping flowrate Q, thus representing the fraction of Q that flows through L1 and L2 ($\frac{\Delta Q_{L1}}{Q}$; $\frac{\Delta Q_{L2}}{Q}$). Along boundary L1 ($x=a$; between D1 and D*), according to Eq. 4 and for the anisotropic case, the solution is:

$$\frac{\Delta Q_{L1}(y,t)}{Q} = \frac{T_1}{Q}\frac{\partial s_1(a,y,t)}{\partial x}$$

$$= \frac{T^*\gamma_0}{\pi(T_1\tau_0 + T^*\gamma_0)}\left\{\frac{a}{a^2+y^2}e^{-\frac{S_1}{4T_1 t}(a^2+y^2)}\right.$$

$$\left. - \tau_0 \sum_{n=2,4,6}^{\infty} \frac{2T_1}{T_1\tau_n + T^*\gamma_n}\prod_{i=1,3,5}^{n-1}\frac{T^*\tau_i - T_2\gamma_i}{T^*\tau_i + T_2\gamma_i}\prod_{i=2,4,6}^{n-2}\frac{T^*\gamma_i' - T_1\tau_i'}{T^*\gamma_i' + T_1\tau_i'} \left(\frac{nh^* + a}{[a+nh^*]^2+y^2}\right)e^{-\frac{S_1}{4T_1 t}([a+nh^*]^2+y^2)}\right\}$$

(11)

and for flow along boundary L2 (x=a+h; between D* and D2), according to Eq. 6 and for the anisotropic case, the solution is:

$$\frac{\Delta Q_{L2}(y,t)}{Q} = \frac{T_2}{Q}\frac{\partial s_2(a+h,y,t)}{\partial x}$$

$$= \frac{T^*\gamma_0\tau_0}{\pi(T_1\tau_0 + T^*\gamma_0)}\left\{\sum_{n=0,2,4}^{\infty} \frac{2T_2\gamma_{n+1}\tau_{n+1}}{T_2\tau_{n+1} + T^*\gamma_{n+1}}\prod_{i=1,3,5}^{n-1}\frac{T^*\tau_i - T_2\gamma_i}{T^*\tau_i + T_2\gamma_i}\prod_{i=2,4,6}^{n}\frac{T^*\gamma_i' - T_1\tau_i'}{T^*\gamma_i' + T_1\tau_i'} \left(\frac{a + h^*(n+1)}{[a+h^*(n+1)]^2+y^2}\right)e^{-\frac{S_2}{4T_2 t}([a+h^*(n+1)]^2+y^2)}\right\}$$

(12)

where $h^* = h\sqrt{\frac{T_y^*}{T_x^*}}$, $T^* = \sqrt{T_x^* T_y^*}$, and where coefficients γ and τ are determined from Eqs. 4 to 6 (h is replaced by $h\sqrt{\frac{T_y^*}{T_x^*}}$, and T* by $\sqrt{T_x^* T_y^*}$). Note that Eq. 11 and Eq. 12 can also be obtained from Eq. 5 (domain D*) at the corresponding boundaries.

5.2. Flux profile along L1 and L2

Equations 11 and 12 are complex functions whose behaviour was explored through numerical experiments. Figures 8a and b show the flow profile along both boundaries (i.e. along the y-axis, with y≥0 both solutions being symmetrical about the x-axis) after 21 days of pumping (t=3x10^4 min and Q=1 m^3/h). For this experiment, the pumping well is located at 10.0 m from a 5-m-wide strip aquifer (a=10.0 m and h=5.0 m). In all cases, the hydraulic properties in D1 are identical (T_1=10^{-3} m^2/s; S_1 =5x10^{-3}). For curves A to F, the properties of D2 are identical

457 to those of D1 (T_1=T_2; S_1=S_2), D* is isotropic but its properties differ, T* varies from $2x10^{-4}$
458 to $2x10^{-2}$ m^2/s and S* from 10^{-3} to $6x10^{-1}$, making compartment D* both the most or the least
459 transmissive, or the most and the least diffusive aquifer. Curve G is similar to C, but D2 is the
460 least transmissive, and storativity is the least (T_2=10^{-4} m^2/s; S_2 =10^{-3}). Curve H differs from G
461 only because D* is anisotropic in transmissivity (T_y*/T_x*=50.0).

462 Analysis of these curves shows that, as mentioned in earlier studies (Abbaszadeh and Cinco-
463 Ley, 1995, Abbaszadeh et al., 2000; Rahman et al., 2003), the flow through boundary L1 is
464 mainly from the compartment D* to D1. Locally, however, it can also be reversed (from D1
465 to D*) when the central compartment D* becomes the most transmissive aquifer (Fig. 8a,
466 curves A, B, C, G and H). This flow reversal indicates that, at a certain distance along the *y*-
467 axis (or from the pumping well) and after a certain duration of pumping, the hydraulic
468 gradient at the boundary between D1 and D* is reversed. This implies that streamlines are
469 reversed, because drawdown within the central compartment propagates faster than in the
470 surrounding compartments. Such behaviour stems from the higher transmissivity in D*, but
471 not necessarily because of a higher diffusivity (curves: A, B). For curve E, D* is the most
472 diffusive, but reversed flow is absent. Curve A presents the equal diffusivity ratio case in
473 which flow reversal occurs. Regarding the storativity (*S**), the higher the value, the greater the
474 reversed flow (curves: A, B, C). When compartment D2 on the right-side is the least
475 transmissive (curves G and H), the flow in D* and therefore the reversed flow (D1 to D*)
476 increase, and an increase in transmissivity anisotropy of D* ($T_y^* > T_x^*$) enhances the flow
477 reversal (curve H). When D2 is the least transmissive, reversed flow may occur even if $T^* \leq T_1$,
478 but with $T^* \geq T_2$ (not shown on the figure), the increase in anisotropy of D* ($T_y^* > T_x^*$) will still
479 increase such flow. Logically, when D* is the least transmissive, no reversed flow will occur
480 (curves: D, E, F), as well as when T_2 becomes the most transmissive aquifer (not shown on
481 the figure).

482 Other tests concerned the distance between the pumping well and L1 (*a*), and the width of the
483 central compartment (*h*). They showed that, regarding distance '*a*', the greater the distance,
484 the greater the influence of pumping on the pumped compartment (D1), and therefore the less
485 on D* and D2. Therefore, logically, flows along the two discontinuities are reduced as '*a*'
486 increases. An increase in the width of the central compartment (*h*) induces an increase in the
487 lateral transmissivity of the central compartment, perpendicular to the *x*-axis, which facilitates
488 the propagation of drawdown in this direction, to the detriment of the *y*-axis. Consequently,

drawdown within the aquifer of the central strip aquifer propagates less rapidly, reducing the reversal hydraulic gradient between D1 and D*, and therefore the reversed flow.

Flow along boundary L2 (between D* and D2) is less complex as it is always positive, from D2 to D* (Fig. 8b). It increases when D* is the least transmissive compartment (curves: D, E, F), and decreases when D* is the most transmissive or anisotropic (with $Ty^*>Tx^*$) compartment (curves: A, B, C, H), or when D2 is the least transmissive (curves G and H). Logically, when D2 is the most transmissive compartment, flow increases (not shown on the figure).

5.3. Time-variation of flux along L1 and L2

Figures 9a and b show the evolution of flow profiles through both boundaries for case H on Figure 8 (the anisotropic case T^*_y/T^*_x=50.0), at time of pumping t=1, 7, 30, 200, 500, $3x10^3$, $3x10^4$ and 10^8 min. Up until 30 min, the flow at boundary L1 is only from compartment D* to D1, as the hydraulic gradient between D1 and D* is always positive. During this period, particularly from about 2 min, when drawdown begins to reach L1, to 30 min, drawdown does not propagate more rapidly in D1 than in D*. From t=30 min the flow reversal starts, as the drawdown begins to propagate faster in D*. The location of the point of reversed flow into/from D*, increases slightly with time. At t=200 min the reversal point is at about 48.0 m, and then converges to about 58 m (y=58.0 m at t=10^8 min). Along L2, the flow from D2 to D* increases with time, particularly for the smallest values of y ($0 \le y \le 150$-200 m; t=1, 7 and 30 min). Then, it flattens for longer time values, but total flow increases significantly. In fact, after 200 min, linear to bi-linear flow regimes start to occur in D* (Fig. 10c), which means that D* begins to drain the two surrounding aquifers (D2 and D1).

The precise assessment of flow along L1 (Eq. 11; Figs. 7a and 8a) is a challenging task. It requires separation of the two flow components, the one from D* to D1 (positive flow), and the one from D1 to D* (negative or reversed flow). This implies separating the positive and negative values of the calculation of Eq. 11. The flow at each time t can be calculated by integrating Eq. 11 along the y-axis at the appropriate interval. For flow from D* to D1, the solution is:

$$\frac{\Delta Q_{L1}(t)}{Q} = 2\int_0^{y_f} \frac{\Delta Q_{L1}}{Q}\, dy \qquad (13)$$

and the one from D1 to D* (flow reversal), is:

$$\frac{\Delta Q_{L1}(t)}{Q} = 2\int_{y_f}^{\infty} \frac{\Delta Q_{L1}}{Q} dy \quad (14)$$

where $\frac{\Delta Q_{L1}}{Q}$ is given by Eq. 11 and y_f is the location of the point of reversed flow into/from compartment D* onto the *y*-axis. However, no formal solution of the roots of Eq. 11 was found, and they were evaluated numerically using the Newton-Raphson method.

For flow along L2, entering compartment D* from D2, Eq. 12 has to be integrated along L2 ($-\infty<y<\infty$), which gives:

$$\frac{\Delta Q_{L2}(t)}{Q} = 2\int_{0}^{+\infty} \frac{\Delta Q_{L2}}{Q} dy \quad (15)$$

where $\frac{\Delta Q_{L2}}{Q}$ is given by Eq. 12.

Note that all integrals in Eqs. 13 to 15 are multiplied by two, to account for symmetrical properties of equations about the *x*-axis. Net flow from Domain D* is obtained by subtracting Eq. 13 from both Eqs. 14 and 15.

Figure 10a shows the variations of the various flow components over time, for the anisotropic example given in Fig. 9 (T^*_y/T_x^*=50.0) and for the case where the compartment D* is isotropic (T^*_y/T_x^*=1.0; all other parameters remaining unchanged). Figure 10b presents the net flow from the strip-aquifer D* (net flow=Eq. 13-[Eq. 14+Eq. 15]). Figure 10c shows the corresponding drawdowns and their derivatives at the pumping well. Flow entering D1 from D*, or the one entering D* from D1 (flow reversal), increases sharply once drawdown begins to propagate significantly in D* (-1 or negative slope on derivatives). Then, once the bi-linear to linear flow regime is established in D* (t>100 min; Fig. 10c), and drawdown propagates in the right-side compartment (D2), the flow along L1 increases and then slows down, almost stabilizing over long times when the whole system responds to pumping (second radial flow regime). The contribution of the strip-aquifer to compartment D1 varies over time (net flow, Fig. 10b) according to the various flow components. It first increases rapidly due to the contribution of D* to D1 (positive flow) and then, once the feature begins to drain the system, it decreases as reversed flow and flow from D2 increase. Logically, an increase of the anisotropy ratio in D* increases the net contribution of D*.

6. Extension of the proposed theory to a well intersecting and pumping a vertical fracture of finite length located near an infinite fault

We propose drawdown solutions for the case of a well intersecting and pumping a vertical fracture of finite length, 2*l*, making an angle α with the *x*-axis (Fig. 1b; Fig. 11) near an infinite vertical discontinuity. They are based on the drawdown solutions for the three compartments developed above for the isotropic and anisotropic cases. The pumping well is located at the centre of the fracture, at a distance *a* from L1. The fracture fully penetrates the aquifer, and should not cross domain D* (i.e. $l\cos\alpha \leq a$). Assuming that the pumping rate *Q* is uniformly distributed along the fracture, i.e. the rate of pumping per unit length of the fracture is $q(x,y) = {}^{Q}/_{2l}$, according to Dewandel et al. (2018), drawdown solutions can be obtained by integrating the above solutions along the fracture axis. Solutions for the three domains then take the following general form:

$$s_{frac}(x,y,t) = \int_{-l}^{+l} s(x,y,t)\,d\vartheta \qquad (16)$$

where $s(x,y,t)$ corresponds to Eqs. 4, 5 or 6 for the isotropic case, which, combined with Eqs. 7, 8 or 9 gives the solutions for the anisotropic case (or $T^*_y/T^*_x \neq 1$). Note that for the particular case where the distance of the pumped fracture to L1 is infinite ($a \to \infty$; i.e. there is only one aquifer system, D1), Eq. 16 corresponds exactly to a known analytical solution (Gringarten et al. (1974), their Eq. 20) for drawdown in a well pumping a vertical fracture with uniform flux distribution that fully penetrates the aquifer (Dewandel et al., 2018).

The integral in Eq.16 can be evaluated numerically with the Gauss-Legendre quadrature, as done here, or evaluated using a discretized form of Eq. 16 by dividing the fracture into small elements and placing the appropriate line-source solution at the centre of each segment (Dewandel et al., 2018, their Eq. 7).

6.1. Drawdown and flow behaviours at the pumping well

Figure 11 presents the result of Eq. 16 for a pumping well of radius r_w intercepting a fracture parallel to domain D* (i.e. parallel to the *y*-axis, α=90°). Dimensionless time according to fracture length, $t_{Df} = T_1 t/(S_1 l^2)$, and dimensionless drawdown, $s_{Df}\left({}^{a}/_{l}, t_{Df}\right) = \frac{2\pi T_1}{Q} s_{pwf}(r_w, t)$, are used for presenting the case where T_1/S_1=0.1, $T^*/S^* = T_2/S_2$=0.5, T^*_y/T^*_x=10.0, T^*/T_1=100.0; T_1/T_2=20.0, *h*= 5 m, and *a*/*l* ratios varying from 1 to 10. This setting describes the behaviour of a fracture with increasing distance from boundary L1.

At the start of pumping, the flow is linear (half-unit slope of derivative curves) and corresponds to flow from aquifer D1 to the fracture intersected by the pumping well. For intermediate pumping stages, the derivative curves may describe the first infinite-acting radial flow, when both the boundary L1 has not yet been reached by pumping and the fracture is far enough from L1, $a/l>4$. For this case, $\partial s_{Df}/\partial Ln(t_{Df}) = 1/2$ or $\partial s_{frac}/\partial Ln(t) = Q/4\pi T_1$). Then, once the cone of depression begins to reach boundary L1, the derivative slope decreases, and may tend to -1 when the half-fracture size is close to the distance between the centre of the fracture and L1 ($a/l\leq 3$). This shows that D* acts temporarily as a steady-state source. At times $t_{Df}>10.0$ derivatives follow a near ¼ slope, describing the earlier-mentioned bi-linear flow regime within domain D*. As for the case of pumping in a well (without fracture), the derivative slope may also tend to ½ when S^*/S_1 ratios are high (linear flow regime within D*). For late pumping stages ($t_{Df}>2.10^5$ in Fig. 11), the drawdown has diffused through the whole domain D* and propagates significantly into the right-side aquifer (domain D2), indicating that D* drains the whole aquifer system. A second radial flow regime is encountered and characterizes the overall response of the aquifer system, the derivative always tending to $\frac{2T_1}{T_1+T_2}$ (or $\frac{\partial s_{frac}}{\partial Ln(t)} = Q/[2\pi(T_1+T_2)]$), as in previous solutions (see section 3., above).

6.2. Flow along and through boundaries L1 and L2

As done previously for pumping in a well (without fracture), flow along and across both boundaries L1 and L2 can also be computed using the same procedure as described before (section 5.). Figures 12 and 13 show examples of flow profiles along L1 and L2 at $t=3\text{x}10^4$ min, and time-variations of fluxes along L1 and L2, respectively, for pumping in a 20-m-long fracture ($2l=20$ m) either parallel ($\alpha=90°$), perpendicular ($\alpha=0°$), or making a 45° angle with compartment D* ($\alpha=45°$). In all cases, the aquifer properties in all three compartments are identical to case H in Fig. 8 ($T_1=10^{-3}$ m^2/s, $S_1=5\text{x}10^{-3}$, $T^*=2\text{x}10^{-2}$ m^2/s, $S^*=10^{-2}$, $T^*y/T^*x=50.0$, $T_2=10^{-4}$ m^2/s, $S_2=10^{-3}$, $h=5$ m, $a=10$ m, $Q=1$ m^3/h). The results are also compared to the case where the well that is pumped does not intersect a fracture.

For pumping in a fracture, flow profiles along both boundaries L1 and L2 have a similar shape compared to the case of pumping in a well, and are logically symmetric to the *y*-axis when the fracture is symmetric to the *y*-axis ($\alpha=0°$ and 90°; Fig. 12). Compared to pumping in a well, flow along boundary L1 (Fig. 12a) is higher near the *x*-axis ($x=0$) when the fracture

is perpendicular to D* (α=0°), and is logically less important when it is parallel to it (α=90°). When the fracture makes a secant angle with D* (α=45°), maximum flow shifts to the side where the fracture is closer to boundary L1 (here, to the right). Reversed flow (from D1 to D*) is similar in all cases, including the pumping well case, as the reversal point is far from the fracture, at about 50 m.

Concerning flow along boundary L2 (Fig. 12b), the same remarks apply, except that for the fracture cases flux distribution is characterized by a sharp distribution almost centred along the *x*-axis (near x=0), and is locally higher than that for the well case. This shows that pumping in a fracture concentrates flow in a larger area, and then solicits more compartment D2 near the fracture.

When pumping a fracture, time-variations of flow show similar behaviour to that of the pumping well case (Fig. 13a). In particular, flow reversal is almost identical for all cases. The main difference compared to the pumping well case occurs when the fracture makes a secant angle with D* (α=0 and 45°), forcing D*, but also D2, to react more rapidly, even at early stages during the linear flow caused by pumping in the fracture (Fig. 13c). However, for late pumping stages, the flow from D* to D1 is less in the cases considering a fracture when compared to the pumping well case. This difference stems from the larger pumped area that facilitates the reaction of D1 near the pumped fracture. Consequently, the net flow from compartment D* to D1 (Fig. 13b) is less important when pumping is done through a fracture.

7. Conclusions

New analytical solutions for drawdown are proposed for a pumping well, and for a well intersecting and pumping a vertical fracture of finite length, near an infinite vertical fault zone or another vertical geological discontinuity (vein, dyke, strip aquifer) with finite width, finite storativity, and finite—and possibly anisotropic—hydraulic conductivity. Consequently, the solutions proposed can relate to a relatively large set of hydrogeological situations. However, the dip of the structure must be close to vertical and long enough (with regard to the pumping duration) to be considered as infinite for a good use of the solutions (see Fig. 1).

The solutions are based on an unconventional application of well-image theory, without limitation on the diffusivity contrast between the aquifer compartments, and considering flow transience within the fault. Solutions were developed for the drawdown in three aquifer

compartments, the pumped compartment, the one within the fault zone, and the compartment on the other side of the fault. The solutions are good approximations of the corresponding partial differential equations, and comparison with numerical simulations showed high accuracy.

Drawdown and flow regimes in the pumping well were analysed in various configurations and, overall, are similar to previous studies, especially when the fault zone is strongly permeable and anisotropic. In the last case and once the cone of depression reaches the fault, the slope of the logarithmic derivative of drawdown in the pumping well tends to -1, showing that the fault temporarily acts as a steady-state source. Later, when the fault begins to drain the whole aquifer system, the derivative follows typical ¼ or ½ slopes, depending upon the contrast in aquifer properties that describe bi-linear to linear flow regimes within the fault zone. For the late stages of pumping, the derivative forms a second radial flow regime that depends upon the average transmissivities of the two external aquifer compartments, but not on the fault zone. The first radial flow is established at an early stage, before the cone of depression reaches the fault zone.

This application of image-well theory fits the need for other well functions, which should be derivable on x to get mathematical expressions of strength coefficients. Therefore, drawdown solutions were developed for a well intersecting and pumping a vertical fracture of finite length located near the same infinite vertical fault zone. In terms of flow regimes, behaviour was similar to the pumping well case, except for early pumping stages when a first linear-flow regime defines the response of the pumped vertical fracture. We also believe that other solutions can be derived for a partially penetrating well, or a partially penetrating fracture pumped by a well, located near a 3-D anisotropic fault using the Hantush and Hantush leaky-well functions (Hantush, 1964, 1966; Dewandel et al., 2014). A 3-D geometry of the pumped fracture could be considered as well.

An interesting point of the proposed solutions is the possibility to derive transient-flow solutions along both sides of the fault zone, and thus net transient flow from the fault itself. Depending on the contrast in aquifer parameters between the three compartments, flow reversal between the fault and the pumped aquifer occurs, as found in previous work, when the fault zone is the most permeable. We show that net flow from the fault into the pumped aquifer increases rapidly during the early pumping stage due to contribution of the fault zone, and then, once the fault begins to drain the system, it decreases as reversed flow and flow from the opposite-side aquifer increase. Logically, an increasing anisotropy of the fault zone

675 increases the net contribution of the fault. When the pumping takes place through a vertical
676 fracture near a fault zone, net flow is less important because the fracture increases the reaction
677 of the pumped compartment, compared to the fault zone and the opposite-side compartment.
678 Furthermore, all results show that the net flow contribution is characterized by strong time-
679 variation that stabilizes by long pumping stages. This may influence the quality of the pumped
680 water, especially when the water quality of the fault zone is different from that where the well
681 is located. Future work should focus on such flow computations in an experimental site, using
682 geochemical data for assessing the origin of water (or fluid) when pumping a well, or one that
683 intersects and pumps a fracture near a vertical geological discontinuity.

684

685 **Acknowledgements**

686 The authors are grateful for a research-sponsorship from BRGM (France) and from the
687 Dem'Eaux Thau Research Project, co-funded by the French Water Agency of Rhône
688 Mediterranean & Corsica (AEMRC), Balaruc-les-Bains city, the Syndicat Mixte du Bassin de
689 Thau (SMBT), Montpellier Méditerranée Métropole, European Funds for Regional
690 Development, the French Ministry for Research, and Occitanie Region (CPER). The authors
691 thank Francisco J. Valdes-Parada (Editor of the journal) and two anonymous reviewers for
692 their useful comments and remarks. The authors are grateful to Dr. H.M. Kluijver for revising
693 the final version of the English text.

694

695 **References**

696 Abbaszadeh M.D., Cinco-Ley H., 1995. Pressure transient behavior in a reservoir with a
697 finite-conductivity fault. SPEFE March 1999; Trans., AIME, , 26-32.

698 Abbaszadeh M., Asakawa K., Cinco-Ley H., Arihara N., 2000. Interference testing in
699 reservoirs with conductive faults or fractures. SPE Reservoir Eval. & Eng. 3 (5), 426-434.

700 Althawad, M.S., 2016. Semi-analytical solution to a fractured well in an asymmetric reservoir
701 with a finite conductivity fault. PhD Thesis in Petroleum Engineering. Heriot-Watt
702 University, Institute of Petroleum Engineering, Edinburgh U-K, May 2016. 189 p.

703 Anderson, E.I., 2000. The method of images for leaky boundaries. Wat. Res., 23, 461-474.

704 Anderson, E.I., 2006. Analytical solutions for a flow to a well through a fault. Adv. in Wat.
705 Ress., 29, 1790-1803.

706 Bear J. and G. Dagan, 1965. The relationship between solutions of flow problems in isotropic
707 and anisotropic soils. J. of Hydrology, 3, 88-96.

708 Bense VF, van Balen RT, De Vries JJ, 2003. The impact of faults on the hydrogeological
709 conditions in the Roer Valley Rift System: an overview. Netherlands J. Geosci; 82(1):317–20.

710 Bixel, H.C., Larkin B.K., van Poollen H.K., 1963. Effect of linear discontinuities on pressure
711 build-up and drawdown behavior. J. of Petr. Techn, August 1963, 885-895.

712 Bourdet, D., Whittle T.M., Dougals, A.A., Pirard V.M., 1983. A new set of type curves
713 simplifies well test analysis, World Oil., 95-106, Gulf Publishing Co., Houston.

714 Bourdet D., Ayoud J.A., Prirard Y.M., 1989. Use of pressure derivative in well-test
715 interpretation. SPE, 293-302.

716 Boussila, A.K., Taib, D., Owayed, J., 2003. Pressure behavior of well near a leaky boundary
717 in heterogeneous reservoirs. SPE 80911, https://doi.org/10.2118/80911-MS

718 Bruggeman, G.A., 1999. Analytical Solutions of Geohydrological Problems. Developments in
719 Water Science 46, Elsevier, The Netherlands, 959 p.

720 Butler, J.J. Jr., Liu W.Z., 1991. Pumping tests in non-uniform aquifers—The linear strip case.
721 J. of Hydrol., 128, 69-99.

722 Caine JC, Evans JP, Forster CB. Fault zone architecture and permeability structure. Geology
723 1996;24(11):1025–8.

724 Cooper, H.H. and C.E. Jacob, 1946. A generalized graphical method for evaluating formation
725 constants and summarizing well field history, Am. Geophys. Union Trans., vol. 27, pp. 526-
726 534.

727 Dewandel, B., Lachassagne, P., Zaidi, F.K., Chandra, S., 2011. A conceptual hydrodynamic
728 model of a geological discontinuity in hard rock aquifers: example of a quartz reef in granitic
729 terrain in South India. J. of Hydrol., 405, 474–487.

730 Dewandel, B., Maréchal, J.C., Bour, O., Ladouche, B., Ahmed, S., Chandra, S., Pauwels H.,
731 2012. Upscaling and regionalizing hydraulic conductivity and efficient porosity at watershed
732 scale in crystalline aquifers. J. of Hydrol., 416-417, 83-97.

733 Dewandel B., Aunay B., Maréchal J.C., Roques C., Bour O., Mougin B. and L. Aquilina,
734 2014. Analytical solutions for analysing pumping tests in a sub-vertical and anisotropic fault
735 zone draining shallow aquifers. J. of Hydrology, 509, 115–131.

736 Dewandel B., S. Lanini, P. Lachassagne, J.-C. Maréchal, 2018. A generic analytical solution
737 for modelling pumping tests in wells intersecting fractures. J. of Hydrology, 559, 89–99,
738 https://doi.org/10.1016/j.jhydrol.2018.02.013.

739 Ehlig-Economides, C.A., 1988. Use of the pressure derivative for diagnosing pressure-
740 transient behavior. J. Petrol. Technol. (October), 1280–1288.

741 Escobar, F. H., Martínez, J. A. & Montealegre-Madero, M., 2013. Pressure transient analysis
742 for a reservoir with a finite-conductivity fault. CT&F - Ciencia, Tecnología y Futuro, 5(2), 5-
743 18.

744 Fenske, P.R., 1984. Unsteady drawdown in the presence of a linear discontinuity. In:
745 Rosenshein, J., Bennett G.D. (Eds.), Groundwater Hydraulics. AGU Water Res. Monogr., 9,
746 125-145.

747 Ferris, J.G., Knowles, D.B., Brown, R.H., Stallman R.W., 1962. Theory of aquifer tests.
748 U.S.G.S. Water-Supply Paper. 1536-E, 69-174.

749 Ferroud A., Rafini S., Chesnaux R., 2019. Using flow dimension sequences to interpret non-
750 uniform aquifers with constant-rate pumping-tests: A review. Journ. of Hydrology X, 1-25.
751 https://doi.org/10.1016/j.hydroa.2018.100003

752 Gringarten, A.C., Henry, J., Ramey, H.J., Raghavan, R., 1974. Unsteady state pressure
753 distributions created by a well with a single infinite conductivity vertical fracture. J. Soc. Petr.
754 Eng. 14, 347–360.

755 Haneberg, W.C., 1995. Steady state groundwater flow across idealized faults. Water Resour
756 Res, 31(7):1815–20.

757 Hantush, M.S., 1964. Hydraulics of wells. In: Chow, V.T. (Ed.), Advances in Hydroscience,
758 vol. 1. Academic Press, New York, NY.

759 Hantush, M.S., 1966. Analysis of data from pumping tests in anisotropic aquifers. J. Geoph.
760 Res. 72, 1709–1720.

761 Kruseman, G.P., de Ridder, N.A., Verweij J.M., 1990. Analysis and evaluation of pumping
762 test data. 2nd ed. Wageningen, The Netherlands. ILRI publication 47, 377p.

763 Lachassagne P., Wyns, R., Dewandel B., 2011. The fracture permeability of Hard Rock
764 Aquifers is due neither to tectonics, nor to unloading, but to weathering processes. Terra
765 Nova, 23, 145–161, 2011.

766 Lachassagne P., Dewandel B., Wyns R. 2021. Review: Hydrogeology of weathered
767 crystalline/hard-rock aquifers—guidelines for the operational survey and management of their
768 groundwater resources. 1-34. Hydrog. Journ. https://doi.org/10.1007/s10040-021-02339-7

769 Perrin J., Ahmed S., Hunkeler D., 2011. The role of geological heterogeneities and
770 piezometric fluctuations on groundwater flow and chemistry in hard-rock, southern India.
771 Hydrogeology J. 19 (6), 1189–1201. http://dx.doi.org/10.1007/s10040-011-0745-y.

772 Maréchal J.C., Ladouche B., Dewandel B., Fleury P., Dörfliger N., 2014. Diagnostic Plots
773 Applied to Well-Tests in Karst Systems. J. Mudry et al. (eds.), H2Karst Research in
774 Limestone Hydrogeology, Envir. Earth Science, doi:10.1007/978-3-319-06139-9_9.

775 Maslia M.L., Prowell D.C., 1990. Effect of faults on fluid flow and chloride contamination in
776 a carbonate aquifer system. J Hydrol;115: 1–49.

777 Maximov, V.A., 1962. Unsteady flow of compressible fluid to wells in a heterogeneous
778 medium. Appl. Mech. Tech. Phys. 3, 109–112 (in Russian).

779 Neuman, S.P., Walter, G.R., Bentley, H.W., Ward, J.J., Gonzalez, D.D., 1984. Determination
780 of horizontal aquifer anisotropy with three wells. Ground Water 22, 66–72.

781 Nind, T.E.W., 1965. Influence of absolute and partial hydrogeologic barriers on pump test
782 results. Can. J. Earth Sci. 2, 309–323.

783 Rafini, S., Larocque, M., 2009. Insights from numerical modeling on the hydrodynamics of
784 non-radial flow in faulted media. Adv. Water Resour. 32, 1170–1179.
785 https://doi.org/10.1016/j.advwatres.2009.03.009.

786 Rafini, S., Larocque M.,, 2012. Numerical modeling of the hydraulic signatures of horizontal
787 and inclined faults. Hydrogeol. J., 20, 337–350.

788 Raghavan, R., 2004. A review of applications to constrain pumping test responses to improve
789 on geological description and uncertainty. Rev. of Geoph., 42, 1-29.

790 Raghavan, R., 2010. A composite system with a planar interface. J. Petrol. Sci. Eng. 70, 229–
791 234.

792 Ramey, H.J., 1975. Interference analysis for anisotropic formations – a case history. J. Petr.
793 Techn., 1290–1298.

794 Renard, Ph., Glenz, D., Mejias, M., 2009. Understanding diagnostic plots for well-test
795 interpretation. Hydrogeol. J., 17, 589–600.

796 Spane, F.A., Wurstner, S.K., 1993. DERIV: a computer program for calculating pressures
797 derivatives for use in hydraulic test analysis. Ground Water 31, 814–822.

798 Thiéry, D., 2010. Groundwater flow modelling in porous media using MARTHE. In: Tanguy,
799 J.M. (Ed.), Modelling Software Volume 5. Environmental Hydraulics Series. Editions
800 Wiley/ISTE, London, pp. 45–60.

801 Thiéry, D., 2015. Code de calcul MARTHE - Modélisation 3D des écoulements dans les
802 hydro-systèmes - Notice d'utilisation de la version 7.5, BRGM/RP-64554-FR, Orléans.

803 Thiéry D., Amraoui N., Noyer M.-L., 2018. Modelling flow and heat transfer through
804 unsaturated chalk – Validation with experimental data from the ground surface to the aquifer.
805 J. of Hydrology, 556, 660–673. https://doi.org/10.1016/j.jhydrol.2017.11.041

806 Xiong Y., Xiong W., Cai M., Hou C. a, Wang C., 2017. Laboratory experiments of well
807 testing for fracture-cave carbonate gas reservoirs. Petroleum, 3, 301-308.
808 http://dx.doi.org/10.1016/j.petlm.2016.09.004

809 Xu Y., Hu W., Pang W., 2018. A new method for diagnosing caves in fault-karst carbonate
810 reservoirs. Society of Petroleum Engineers, SPE-192971-MS. 1-8.

811 Yaxley, L.M., 1987. Effect of a partially communicating fault on transient pressure behavior.
812 S.P.E. paper 14311, 60th Annual Fall Meeting, Las Vegas, Nv.

813

List of symbols:

a: distance to boundary L1 in m

e^x: exponential function

h: width of domain D* (linear strip aquifer), in m

l: half-fracture length (in Domain 1), in m

Q: pumping flow rate, in m^3s^{-1}

r_w: well radius, in m

S_1, S^*, S_2: storage coefficients of the right-side compartment (D1), the strip aquifer (D*), and the left-side compartment (D2), respectively, dimensionless

s_1, s^*, s_2: drawdown of the right-side compartment (D1), the strip aquifer (D*), and the left-side compartment (D2), respectively, in m

s_{frac}: drawdown for a well intersecting and pumping a vertical fracture, in m

s_D: dimensionless drawdown for pumping in a well; $s_D\left({}^{r_w}/_{a}, t_{DL}\right) = \frac{2\pi T_1}{Q} s_{pw}(r_w, t)$

s_{Df}: dimensionless drawdown for a well intersecting and pumping a vertical fracture; $s_{Df}\left({}^{a}/_{l}, t_{Df}\right) = \frac{2\pi T_1}{Q} s_{pwf}(r_w, t)$

t_{DL}: dimensionless time according to the distance to the boundary (for pumping in a well); $t_{DL} = T_1 t/(S_1 a^2)$

t_{Df}: dimensionless time according to the fracture half-length (for a well intersecting and pumping a vertical fracture); $t_{Df} = T_1 t/(S_1 l^2)$

t: time, in seconds

T_1, T^*, T_2: transmissivity of the right-side compartment (D1), the strip aquifer (D*), and the left-side compartment (D2) respectively, in m^2/s

T^*_x and T^*_y: principal axes of transmissivity anisotropy in the horizontal plane of the strip aquifer (D*), in m^2/s

x, y: coordinates of a Cartesian system, in m

$W(u) = \int_u^\infty \frac{e^{-\varepsilon}}{\varepsilon} d\varepsilon$ with ε a variable of integration. Well function.

α: angle of the fracture with the x-axis, radian

Appendices

Appendix A *Partial differential equation*

In D1 (Bixel et al., 1963; Butler and Liu, 1991):

$$\frac{\partial^2 s_1}{\partial x^2}+\frac{\partial^2 s_1}{\partial y^2}+\frac{Q}{T_1}\delta(x)\delta(y)=\frac{S_1}{T_1}\frac{\partial s_1}{\partial t}. \quad (A.1)$$

$\delta(x)\delta(y)$ is a combination of Dirac delta functions representing the pumping well as a line source at x=y=0.

In D* (Butler and Liu, 1991):

$$\frac{\partial^2 s^*}{\partial x^2}+\frac{\partial^2 s^*}{\partial y^2}=\frac{s^*}{T^*}\frac{\partial s^*}{\partial t} \quad (A.2)$$

And in D2 (Butler and Liu, 1991):

$$\frac{\partial^2 s_2}{\partial x^2}+\frac{\partial^2 s_2}{\partial y^2}=\frac{S_2}{T_2}\frac{\partial s_2}{\partial t} \quad (A.3)$$

Appendix B ***Calculation of strength coefficients for the first series of image-wells according to boundaries L1 and L2 (Fig. 3a)***

We first consider the first image according to L1 (boundary between D1 and D*; Fig. 3a). In this case, the problem refers to the influence of a partial hydrologic barrier on a well test (Bixel et al.,1963; Fenske, 1984; Maximov, 1962; Nind, 1965; Raghavan, 2010).

Applying the first boundary condition, it results that drawdown in Domain 1 is:

$$s_1(x,y,t)=\frac{Q}{4\pi T_1}\left[\mathrm{W}\left(\frac{S_1}{4T_1 t}(x^2+y^2)\right)+\alpha_0\mathrm{W}\left(\frac{S_1}{4T_1 t}([2a-x]^2+y^2)\right)\right] \quad (B.1)$$

and that drawdown in Domain D* is:

$$s^*(x,y,t)=\frac{Q}{4\pi T^*}\beta_0\mathrm{W}\left(\frac{s^*}{4T^* t}(x^2+y^2)\right) \quad (B.2)$$

Equating Eqs. (B.1) and (B.2), and for the condition x=a (i.e. $s_1(a,y,t)=s^*(a,y,t)$) at the boundary L1, we obtain:

$$1+\alpha_0=\frac{T_1}{T^*}\frac{\beta_0}{\gamma_0} \text{ with } \gamma_0=\frac{\mathrm{W}\left(\frac{S_1}{4T_1 t}(a^2+y^2)\right)}{\mathrm{W}\left(\frac{s^*}{4T^* t}(a^2+y^2)\right)} \quad (B.3)$$

Then, applying the second boundary condition at boundary L1, $T_1 \frac{\partial s_1(a,y,t)}{\partial x} = T^* \frac{\partial s^*(a,y,t)}{\partial x}$, gives:

$$1 - \alpha_0 = \frac{\beta_0}{\tau_0} \text{ with } \tau_0 = \frac{\mathrm{e}\left(-\frac{S_1}{4T_1 t}(a^2+y^2)\right)}{\mathrm{e}\left(-\frac{S^*}{4T^* t}(a^2+y^2)\right)} \quad \text{(B.4)}$$

Equating Eqs. (B.3) and (B.4) gives the strength coefficients α_0 and β_0:

$$\alpha_0 = \frac{T_1\tau_0 - T^*\gamma_0}{T_1\tau_0 + T^*\gamma_0} \quad \text{and } \beta_0 = \frac{2T^*\tau_0\gamma_0}{T_1\tau_0 + T^*\gamma_0} \quad \text{(B.5)}$$

This case, which considers a system composed of only two domains (D1 and D*), is exactly the solution proposed by Fenske (1984) for various diffusivity contrasts ($T_1/S_1 \neq T^*/S^*$).

Now, the pumping well must be imaged about the second boundary L2, and it results that drawdown in Domain D* is:

$$s^*(x,y,t) = \frac{Q}{4\pi T^*}\left[\beta_0 \mathrm{W}\left(\frac{s^*}{4T^* t}(x^2+y^2)\right) + \beta_0' \mathrm{W}\left(\frac{s^*}{4T^* t}[(2a-x)^2+y^2]\right)\right] \quad \text{(B.6)}$$

and that drawdown in Domain 2 is:

$$s_2(x,y,t) = \frac{Q}{4\pi T_2}\delta_0 \mathrm{W}\left(\frac{S_2}{4T_2 t}(x^2+y^2)\right) \quad \text{(B.7)}$$

Equating Eqs. (B.6) and (B.7), and for the condition $x=a+h$ ($s_2(a+h,y,t) = s^*(a+h,y,t)$) at the boundary L2, we obtain:

$$\beta_0 + \beta_0' = \frac{T^*}{T_2}\frac{\delta_0}{\gamma_1} \text{ with } \gamma_1 = \frac{\mathrm{W}\left(\frac{S^*}{4T^* t}[(a+h)^2+y^2]\right)}{\mathrm{W}\left(\frac{S_2}{4T_2 t}[(a+h)^2+y^2]\right)} \quad \text{(B.8)}$$

Applying the second boundary condition at boundary L2, $T_2 \frac{\partial s_2(a+h,y,t)}{\partial x} = T^* \frac{\partial s^*(a+h,y,t)}{\partial x}$, gives:

$$\beta_0 - \beta_0' = \frac{\delta_0}{\tau_1} \text{ with } \tau_1 = \frac{\mathrm{e}\left(-\frac{S^*}{4T^* t}[(a+h)^2+y^2]\right)}{\mathrm{e}\left(-\frac{S_2}{4T_2 t}[(a+h)^2+y^2]\right)} \quad \text{(B.9)}$$

Equating Eqs. (B.8) and (B.8) gives the strength coefficients β'_0 and δ_0:

$$\beta_0' = -\beta_0 \frac{T_2\tau_1 - T^*\gamma_1}{T_2\tau_1 + T^*\gamma_1} \text{ and } \delta_0 = \frac{2T_2\tau_1\gamma_1}{T_2\gamma_1 + T^*\tau_1} \quad \text{(B.10)}$$

Calculation of strength coefficients for the second series of image-wells according to L1 and L2 (Fig. 3b).

Drawdown in Domain 1 is:

$$s_1(x,y,t) = \frac{Q}{4\pi T_1}\alpha_1 \mathrm{W}\left(\frac{S_1}{4T_1 t}([2a+2h-x]^2+y^2)\right) \quad \text{(B.11)}$$

Drawdown in Domain D* is:

$$s^*(x,y,t) = \frac{Q}{4\pi T^*}\left[\beta_0' \mathrm{W}\left(\frac{s^*}{4T^* t}([2a+2h-x]^2+y^2)\right) + \beta_0 \mathrm{W}\left(\frac{s^*}{4T^* t}([2h+x]^2+y^2)\right)\right] \quad \text{(B.12)}$$

Drawdown in Domain D2 is:

$$s_2(x,y,t) = \frac{Q}{4\pi T_2}\delta_1 \mathrm{W}\left(\frac{S_2}{4T_2 t}[(2h+x)^2+y^2]\right) \quad \text{(B.13)}$$

Applying the two boundary conditions at each boundary, first at L1 and then at L2, results that strength coefficients α_1, β'_0, β_1, β'_1 and δ_1 are given by:

$$\alpha_1 = \beta_0' \frac{2T_1}{T_1\tau_2+T^*\gamma_2},\ \beta_1 = \beta_0' \frac{T^*\gamma_2 - T_1\tau_2}{T^*\gamma_2+T_1\tau_2},\ \beta_1' = -\beta_1 \frac{T_2\tau_3 - T^*\gamma_3}{T_2\tau_3+T^*\gamma_3} \text{ and } \delta_1 = \beta_1 \frac{2T_2\tau_3\gamma_3}{T_2\gamma_3+T^*\tau_3} \quad \text{(B.14)}$$

with $\gamma_2 = \frac{\mathrm{W}\left(\frac{S_1}{4T_1 t}([a+2h]^2+y^2)\right)}{\mathrm{W}\left(\frac{s^*}{4T^* t}([a+2h]^2+y^2)\right)}$, $\tau_2 = \frac{\mathrm{e}\left(-\frac{S_1}{4T_1 t}([a+2h]^2+y^2)\right)}{\mathrm{e}\left(-\frac{s^*}{4T^* t}([a+2h]^2+y^2)\right)}$, $\gamma_3 = \frac{\mathrm{W}\left(\frac{s^*}{4T^* t}[(a+3h)^2+y^2]\right)}{\mathrm{W}\left(\frac{S_2}{4T_2 t}[(a+3h)^2+y^2]\right)}$ and

$\tau_3 = \frac{\mathrm{e}\left(-\frac{s^*}{4T^* t}[(a+3h)^2+y^2]\right)}{\mathrm{e}\left(-\frac{S_2}{4T_2 t}[(a+3h)^2+y^2]\right)}$.

and so on.

Appendix C *Drawdown solutions for the equal diffusivity case ($T_1/S_1=T^*/S^*=T_2/S_2=\eta$)*

For Domain 1:

$$s_1(x,y,t) =$$

$$\frac{Q}{4\pi T_1}\left\{\mathrm{W}\left(\frac{x^2+y^2}{4\eta t}\right) + \frac{T_1-T^*}{T_1+T^*}\mathrm{W}\left(\frac{[2a-x]^2+y^2}{4\eta t}\right) + \right.$$

$$\left.\left(\frac{-2T^*}{T_1+T^*}\right)\left(\frac{2T_1}{T_1+T^*}\right)\left(\frac{T_2-T^*}{T_2+T^*}\right)\sum_{n=0,1,2}^{\infty}\left(\frac{T_1-T^*}{T_1+T^*}\right)^n\left(\frac{T_2-T^*}{T_2+T^*}\right)^n \mathrm{W}\left(\frac{[2a+2(n+1)h-x]^2+y^2}{4\eta t}\right)\right\} \quad \text{(C.1)}$$

For Domain D*:

$$s^*(x,y,t) = \frac{Q}{4\pi T^*}\left\{\left(\frac{-2T^*}{T_1+T^*}\right)\left(\frac{T_2-T^*}{T_2+T^*}\right)\sum_{n=0,1,2}^{\infty}\left(\frac{T_1-T^*}{T_1+T^*}\right)^n\left(\frac{T_2-T^*}{T_2+T^*}\right)^n \mathrm{W}\left(\frac{[2a+2(n+1)h-x]^2+y^2}{4\eta t}\right) + \left(\frac{2T^*}{T_1+T^*}\right)\sum_{n=0,1,2}^{\infty}\left(\frac{T_1-T^*}{T_1+T^*}\right)^n\left(\frac{T_2-T^*}{T_2+T^*}\right)^n \mathrm{W}\left(\frac{[2nh+x]^2+y^2}{4\eta t}\right)\right\} \quad \text{(C.2)}$$

And for Domain 2:

$$s_2(x,y,t) = \frac{Q}{4\pi T_2}\left(\frac{2T^*}{T_1+T^*}\right)\left(\frac{2T_2}{T_2+T^*}\right)\left\{\sum_{n=0,1,2}^{\infty}\left(\frac{T_1-T^*}{T_1+T^*}\right)^n\left(\frac{T_2-T^*}{T_2+T^*}\right)^n \mathrm{W}\left(\frac{[nh+x]^2+y^2}{4\eta t}\right)\right\} \quad \text{(C.3)}$$

Note that for this particular case, strength coefficients are identical to the ones given by Anderson (2006) for a steady-state solution.

Figure captions

Figure 1. Conceptual sketches: a) of a pumping well and b) of a well intersecting and pumping a vertical fracture with finite length, located near a vertical infinite and anisotropic fault zone, (or another vertical geological discontinuity, strip aquifer). Domain D* (width *h*) separates two semi-infinite half-spaces of dissimilar properties (domains D1 and D2). The pumping well, or the pumped vertical fracture, is located in D1 and is not connected to D*.

Figure 2. Graphical display of the image-well series. (a) Image-well according to L1 and L2, graphical display of the image-well series. (b) Observation well located in domain D1. (c) Observation well located in domain D*. (d) Observation well located in domain D2. Modified from Anderson (2006). The pumping well is located in D1.

Figure 3. Graphical display of the first image-wells and calculation of the corresponding strength coefficients. (a) First series of image-wells according to L1 and L2. (b) Second series of images according to L1 and L2.

Figure 4. Type-curves of dimensionless drawdown (s_D) and derivatives s_D', and dimensionless time (t_{DL}) for a pumping well near a vertical infinite and isotropic fault zone (D*). T_1/S_1=0.1, T_2/S_2=0.5, T_1/T_2=20.0, h= 5 m. (a) Variations of transmissivity contrast T^*/T_1 (10^{-2} to 10^3) with S^*/S_1 =20.0. (b) Variations of storativity contrast S^*/S_1 (10^{-3} to 10^3) with T^*/T_1= 100.0.

Figure 5. Type-curves of dimensionless drawdown (s_D) and derivatives s_D', and dimensionless time (t_{DL}) for a pumping well near a vertical infinite and anisotropic fault zone. Anisotropy ratio varies ($10^{-3} \leq T^*_y/T^*_x \leq 10^3$) T_1/S_1=0.1, S^*/S_1=20.0, $T^*/S^*=T_2/S_2$=0.5, T_1/T_2=20.0, h= 5m.

Figure 6. Comparison of drawdown, s, and derivative, s', computed with MARTHE software (plain dots: s; open dots: s') and the analytical solutions (plain curves: s; dotted curves: s') for the anisotropic case (Eqs. 4-6 with Eqs. 7-9). See figure and text for model parameters. The inserted tables show RMSE values for various observation-well locations (x, y coordinates). (a) Model 1: T^*: 10^{-1} m^2/s and S^*:10^{-1}. (b) Model 2 T^*: $3x10^{-3}$ m^2/s and S^*: $2x10^{-2}$. In both cases, T^*_y/T^*_x=*10.0.* ''

Figure 7. Conceptual sketch of flow behaviour through boundaries L1 and L2, where the transmissivity of the central compartment (D*, fault zone) is higher than that of other compartments. Black arrows: normal flow from compartment D* to D1, or D2 to D*. Blue arrows: flow reversal from D1 to D*. Pumping is performed in D1.

Figure 8. Flow profiles through both discontinuities. (a) L1 and (b) L2 with various aquifer properties after 21 days of pumping (t=3x10^4 min and Q=1 m*3*/h). The pumping well is located at 10.0 m from a 5-m-wide fault zone (a=10.0 m and h=5.0 m). See figure and text for model parameters.

Figure 9. Flow profiles through both discontinuities. (a) L1 and (b) L2 at various times of pumping, t=1, 7, 30, 200, 500, 3x10^3, 3x10^4 and 10^8 min. It corresponds to case H on Figure 7 (the anisotropic case T^*_y/T^*_x=50.0). See figure and text for model parameters.

Figure 10. (a) Time-variations of the various flow components through both discontinuities L1 and L2. (b) Net flow from strip aquifer D*. (c) Corresponding drawdowns and their derivatives at the pumping well. Two examples are shown, the one given on Figure 8 (T^*_y/T_x^*=50.0, case H) and the one where D* is isotropic (T^*_y/T_x*=1.0), all other parameters remaining unchanged.

Figure 11. Type-curves of dimensionless drawdown (s_{Df}) and derivatives s_{Df}', and dimensionless time (t_{Df}) for a well intersecting and pumping a vertical fracture near a vertical infinite and anisotropic strip aquifer (Fig. 1b). Variations of a/l ratios (from 1 to 10), T_1/S_1=0.1, $T^*/S^*=T_2/S_2$=0.5, T^*_y/T^*_x=10.0, T^*/T_1=100.0; T_1/T_2=20.0, h= 5 m.

Figure 12. Flow profiles through both boundaries: (a) L1 and (b) L2 for a well intersecting and pumping a vertical fracture near a vertical infinite fault zone at t=3x10^4 min. T_1=10^{-3} m^2/s, S_1 =5x10^{-3}, T*=2x10^{-2} m^2/s, S*=10^{-2}, T*y/T*x=50.0, T_2=10^{-4} m^2/s, S_2=10^{-3}, h=5 m and a=10 m, Q=1 m^3/h, fracture length 2l=20 m, and α=0°, 45° and 90° (a: angle of the fracture according to the x-axis). We also presented the case where a well is pumped without fracture (grey curve H on Fig. 8).

Figure 13. (a) Time-variations of flux along L1 and L2. (b) Net flow from fault zone D*. (c) Corresponding drawdown and derivatives at a well intersecting and pumping a fracture. Aquifer properties are identical to the examples shown on Fig. 12. We also present the case where a well is pumped, without fracture (in grey, the same as on Fig. 9).

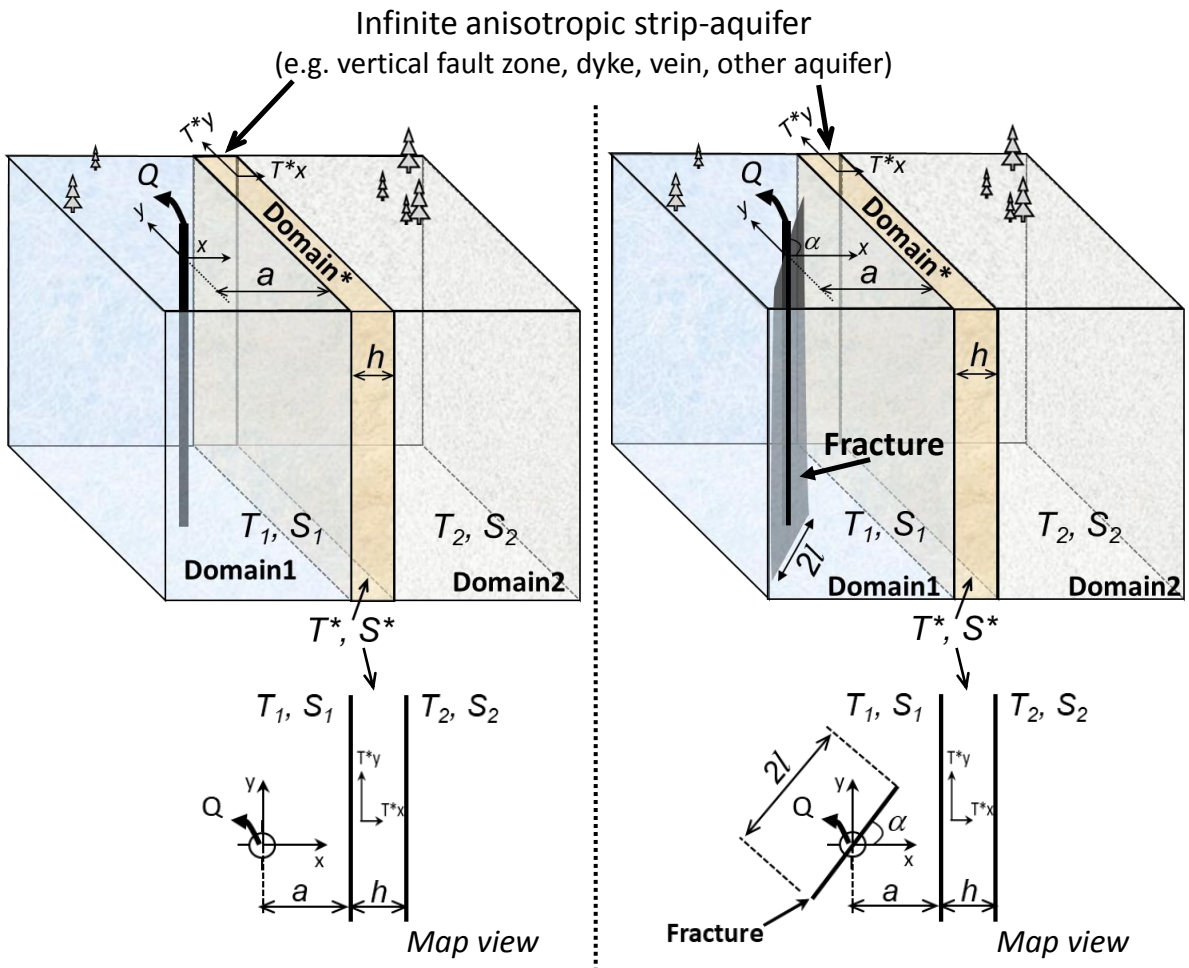

a) Pumping in a well

b) Pumping in a well intersecting a vertical fracture with finite length

Figure 1

971

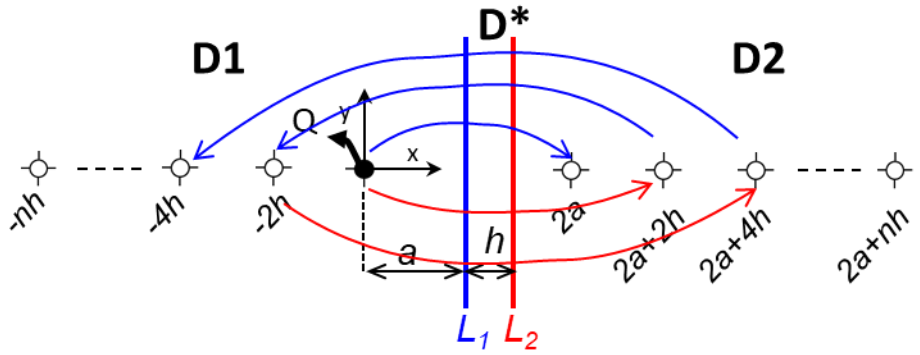

(a) Image-wells according to boundaries L1 and L2

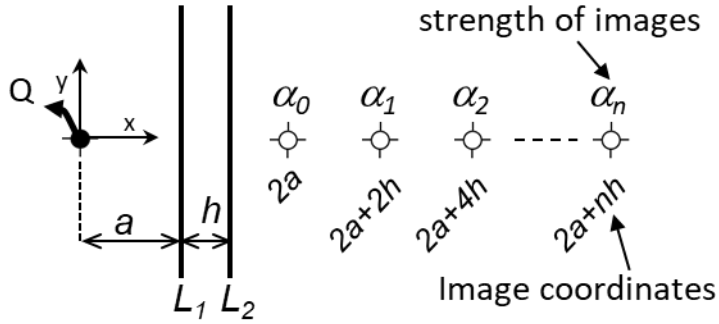

(b) For an observation well located in Domain 1

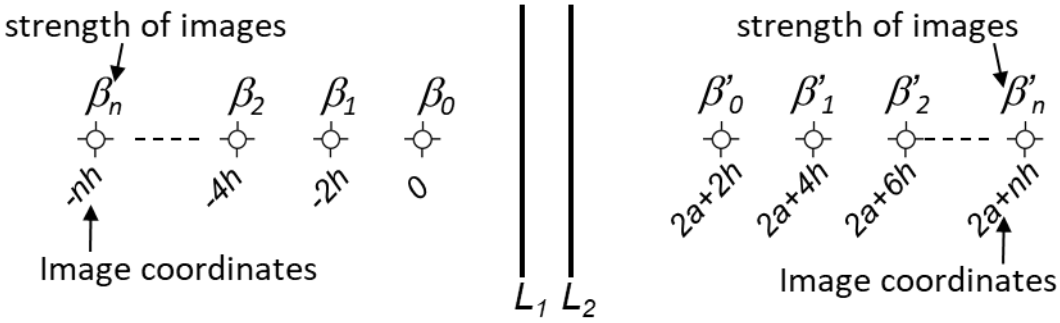

(c) for an observation well located in Domain *

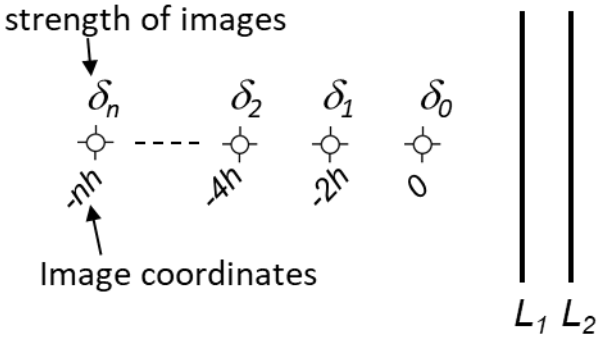

(d) for an observation well located in Domain 2

Figure 2

972

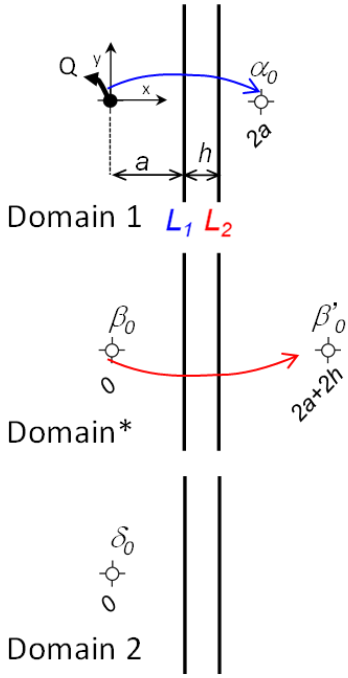

strength of image for $s_1(x,y,t)$

$$\alpha_0 = \frac{T_1\tau_0 - T^*\gamma_0}{T_1\tau_0 + T^*\gamma_0}$$

strength of images for $s^*(x,y,t)$

$$\beta_0 = \frac{2T^*\tau_0\gamma_0}{T_1\tau_0 + T^*\gamma_0}$$

$$\beta'_0 = -\beta_0\frac{T_2\tau_1 - T^*\gamma_1}{T_2\tau_1 + T^*\gamma_1}$$

strength of image for $s_2(x,y,t)$

$$\delta_0 = \frac{2T_2\tau_1\gamma_1}{T_2\gamma_1 + T^*\tau_1}$$

With

$$\gamma_0 = \frac{W\left(\frac{S_1}{4T_1t}(a^2+y^2)\right)}{W\left(\frac{s^*}{4T^*t}(a^2+y^2)\right)}$$

$$\tau_0 = \frac{e\left(-\frac{S_1}{4T_1t}(a^2+y^2)\right)}{e\left(-\frac{s^*}{4T^*t}(a^2+y^2)\right)}$$

$$\gamma_1 = \frac{W\left(\frac{S^*}{4T^*t}[(a+h)^2+y^2]\right)}{W\left(\frac{S_2}{4T_2t}[(a+h)^2+y^2]\right)}$$

$$\tau_1 = \frac{e\left(-\frac{S^*}{4T^*t}[(a+h)^2+y^2]\right)}{e\left(-\frac{S_2}{4T_2t}[(a+h)^2+y^2]\right)}$$

(a) first series of image-well according to L1 and L2

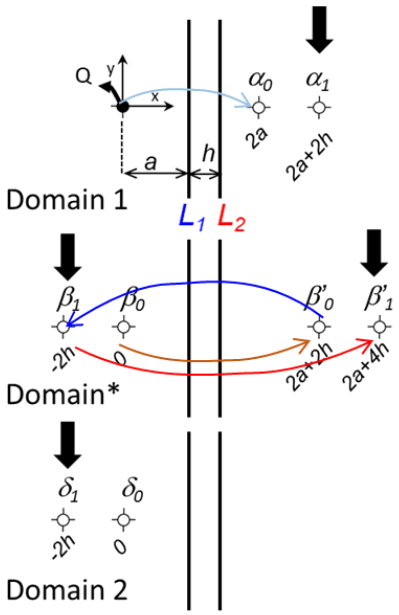

strength of image for $s_1(x,y,t)$

$$\alpha_1 = \beta'_0\frac{2T_1}{T_1\tau_2 + T^*\gamma_2}$$

strength of images for $s^*(x,y,t)$

$$\beta_1 = \beta'_0\frac{T^*\gamma_2 - T_1\tau_2}{T^*\gamma_2 + T_1\tau_2}$$

$$\beta'_1 = -\beta_1\frac{T_2\tau_3 - T^*\gamma_3}{T_2\tau_3 + T^*\gamma_3}$$

strength of image for $s_2(x,y,t)$

$$\delta_1 = \beta_1\frac{2T_2\tau_3\gamma_3}{T_2\gamma_3 + T^*\tau_3}$$

With

$$\gamma_2 = \frac{W\left(\frac{S_1}{4T_1t}([a+2h]^2+y^2)\right)}{W\left(\frac{s^*}{4T^*t}([a+2h]^2+y^2)\right)}$$

$$\tau_2 = \frac{e\left(-\frac{S_1}{4T_1t}([a+2h]^2+y^2)\right)}{e\left(-\frac{s^*}{4T^*t}([a+2h]^2+y^2)\right)}$$

$$\gamma_3 = \frac{W\left(\frac{S^*}{4T^*t}[(a+3h)^2+y^2]\right)}{W\left(\frac{S_2}{4T_2t}[(a+3h)^2+y^2]\right)}$$

$$\tau_3 = \frac{e\left(-\frac{S^*}{4T^*t}[(a+3h)^2+y^2]\right)}{e\left(-\frac{S_2}{4T_2t}[(a+3h)^2+y^2]\right)}$$

(b) second series of images according to L1 and L2

Figure 3

973

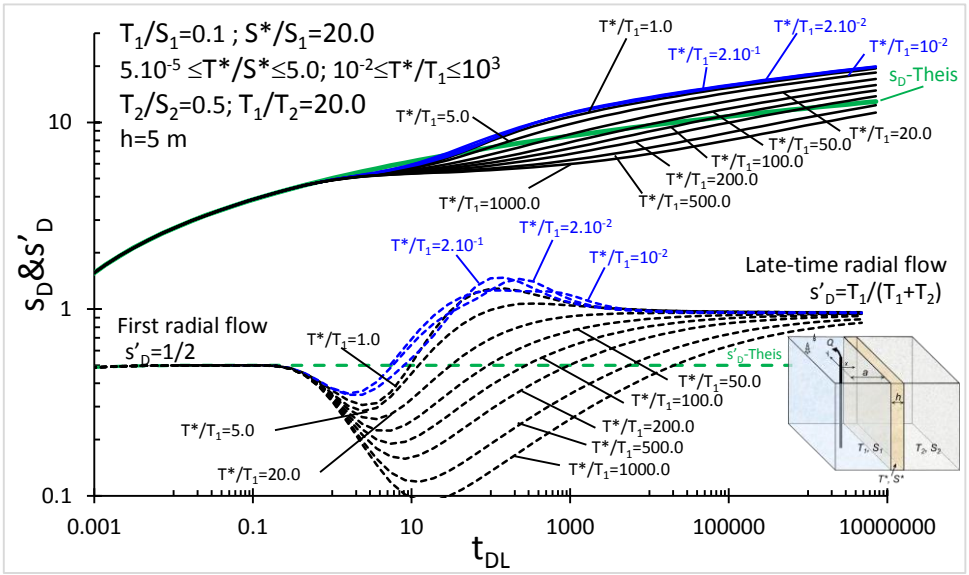

(a)

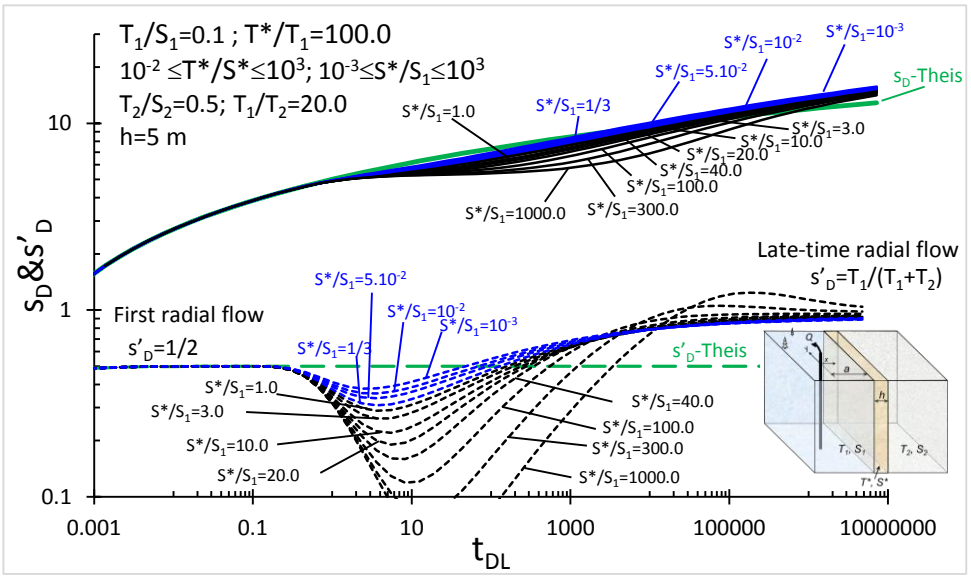

(b)

Figure 4

974

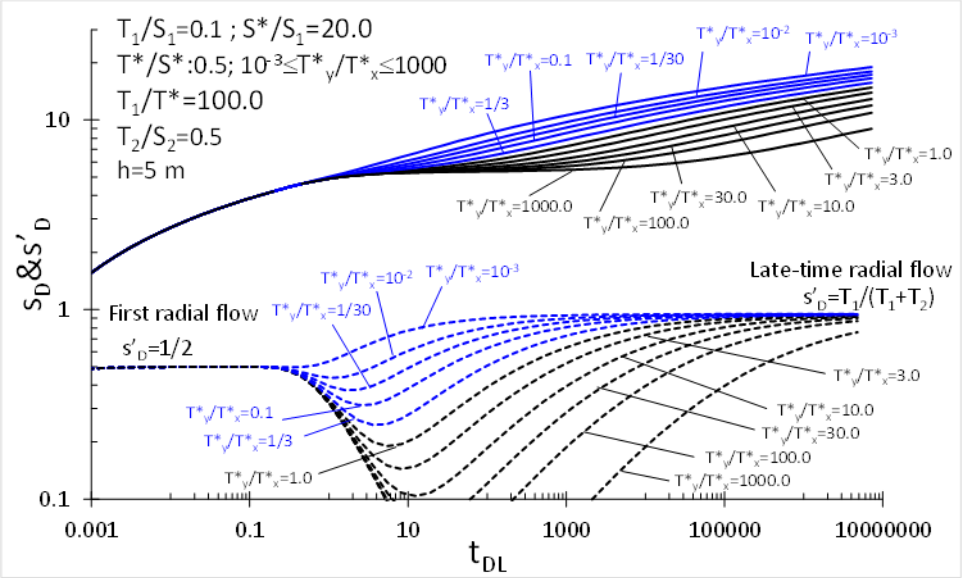

Figure 5

975

976

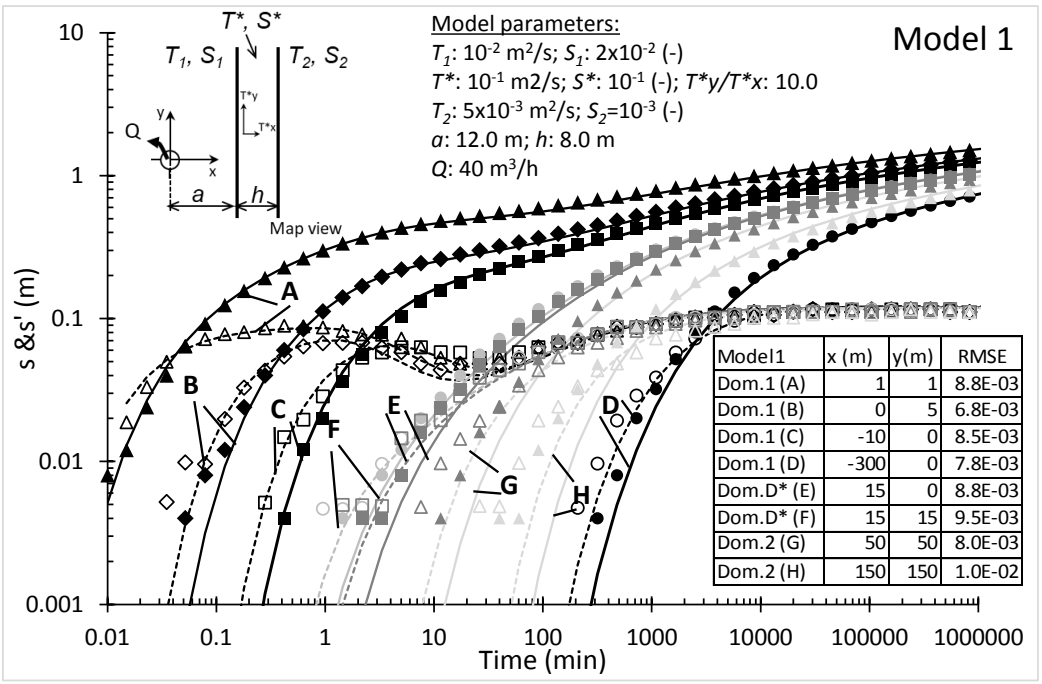
Model 1
Model parameters:
T_1: 10^{-2} m²/s; S_1: $2x10^{-2}$ (-)
T^*: 10^{-1} m2/s; S^*: 10^{-1} (-); T^*y/T^*x: 10.0
T_2: $5x10^{-3}$ m²/s; S_2=10^{-3} (-)
a: 12.0 m; h: 8.0 m
Q: 40 m³/h
T*, S*
T1, S1
T2, S2
Map view
s &s' (m)
Time (min)
A
B
C
D
E
F
G
H
Model1 | x (m) | y(m) | RMSE
Dom.1 (A) | 1 | 1 | 8.8E-03
Dom.1 (B) | 0 | 5 | 6.8E-03
Dom.1 (C) | -10 | 0 | 8.5E-03
Dom.1 (D) | -300 | 0 | 7.8E-03
Dom.D* (E) | 15 | 0 | 8.8E-03
Dom.D* (F) | 15 | 15 | 9.5E-03
Dom.2 (G) | 50 | 50 | 8.0E-03
Dom.2 (H) | 150 | 150 | 1.0E-02

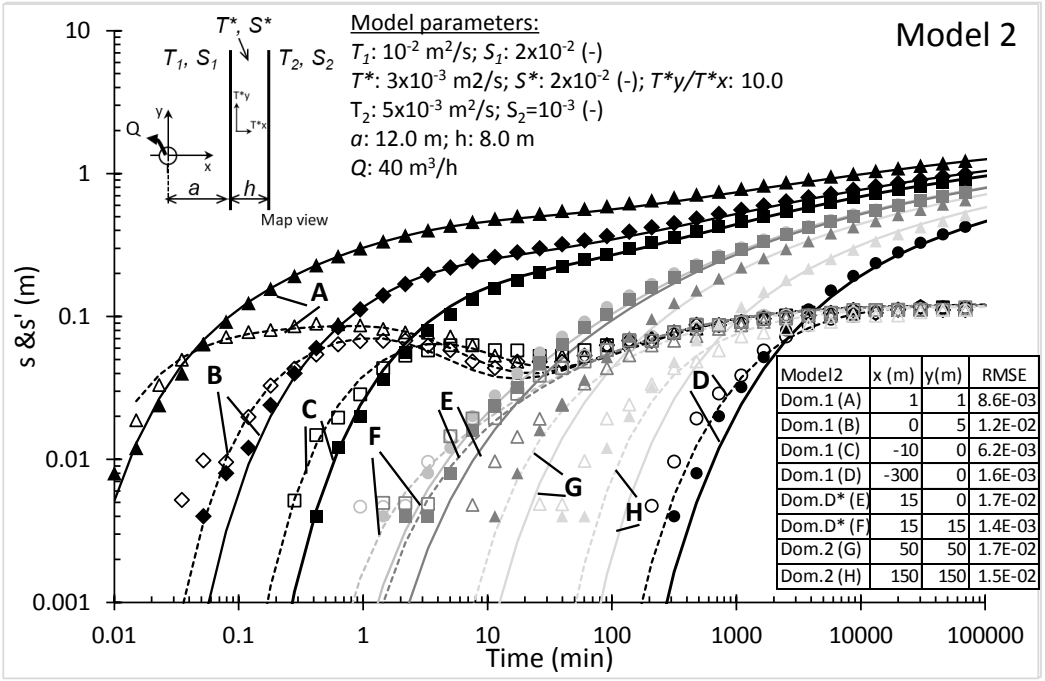
Model 2
Model parameters:
T_1: 10^{-2} m²/s; S_1: $2x10^{-2}$ (-)
T^*: $3x10^{-3}$ m2/s; S^*: $2x10^{-2}$ (-); T^*y/T^*x: 10.0
T_2: $5x10^{-3}$ m²/s; S_2=10^{-3} (-)
a: 12.0 m; h: 8.0 m
Q: 40 m³/h
T*, S*
T1, S1
T2, S2
Map view
s &s' (m)
Time (min)
A
B
C
D
E
F
G
H
Model2 | x (m) | y(m) | RMSE
Dom.1 (A) | 1 | 1 | 8.6E-03
Dom.1 (B) | 0 | 5 | 1.2E-02
Dom.1 (C) | -10 | 0 | 6.2E-03
Dom.1 (D) | -300 | 0 | 1.6E-03
Dom.D* (E) | 15 | 0 | 1.7E-02
Dom.D* (F) | 15 | 15 | 1.4E-03
Dom.2 (G) | 50 | 50 | 1.7E-02
Dom.2 (H) | 150 | 150 | 1.5E-02

Figure 6

977

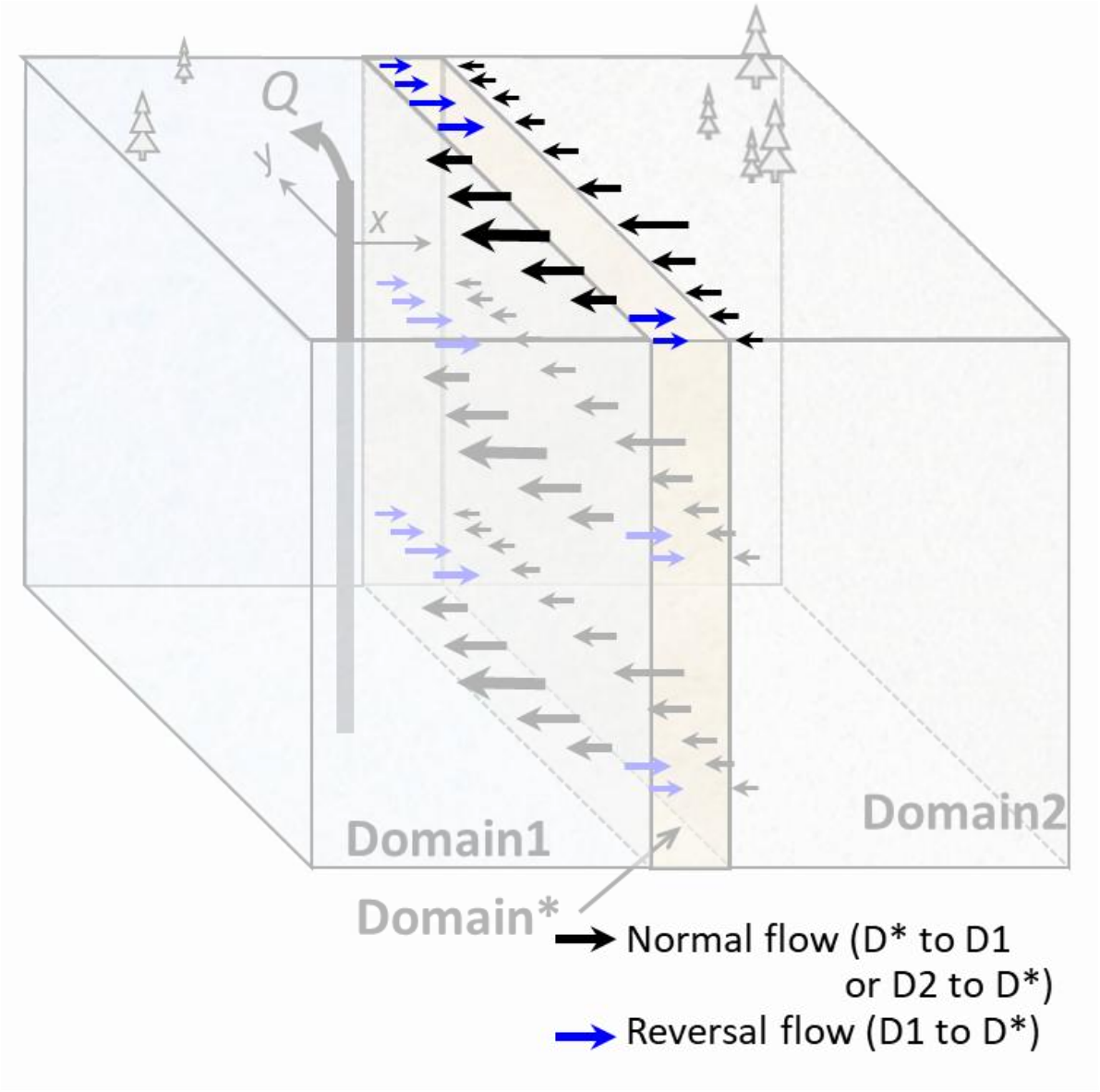

Figure 7

978

979

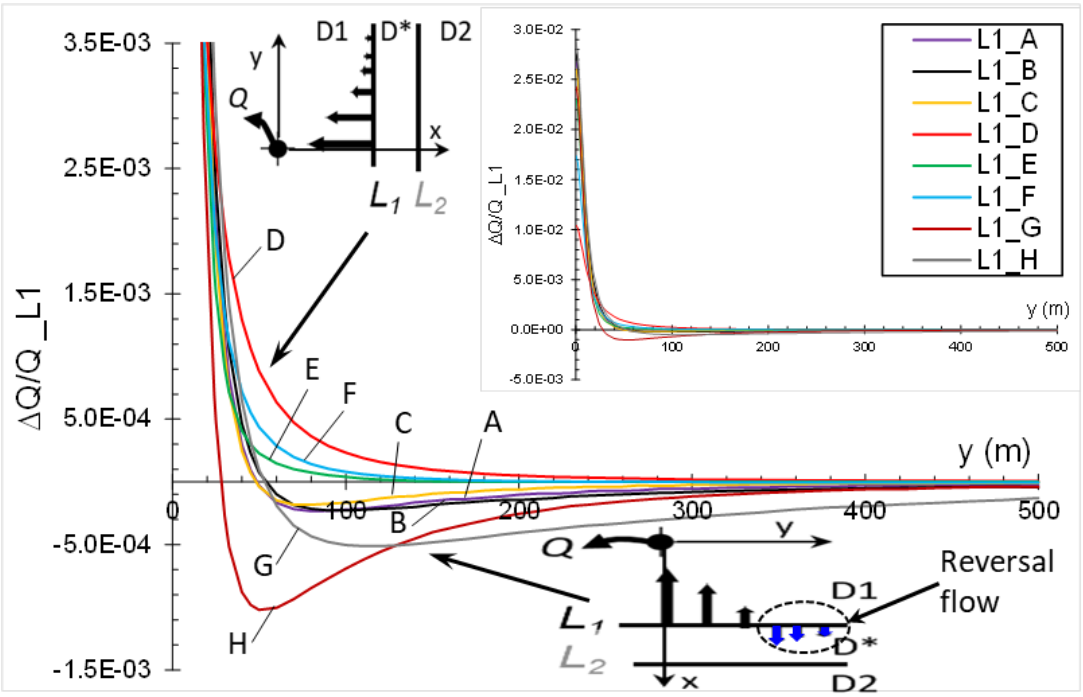

(a)

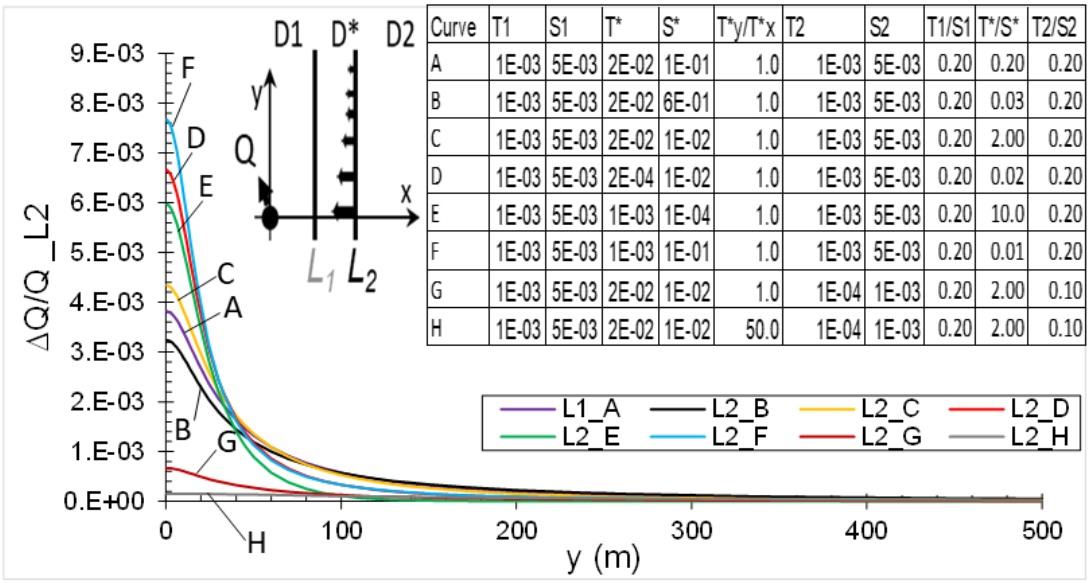

Curve	T1	S1	T*	S*	T*y/T*x	T2	S2	T1/S1	T*/S*	T2/S2
A	1E-03	5E-03	2E-02	1E-01	1.0	1E-03	5E-03	0.20	0.20	0.20
B	1E-03	5E-03	2E-02	6E-01	1.0	1E-03	5E-03	0.20	0.03	0.20
C	1E-03	5E-03	2E-02	1E-02	1.0	1E-03	5E-03	0.20	2.00	0.20
D	1E-03	5E-03	2E-04	1E-02	1.0	1E-03	5E-03	0.20	0.02	0.20
E	1E-03	5E-03	1E-03	1E-04	1.0	1E-03	5E-03	0.20	10.0	0.20
F	1E-03	5E-03	1E-03	1E-01	1.0	1E-03	5E-03	0.20	0.01	0.20
G	1E-03	5E-03	2E-02	1E-02	1.0	1E-04	1E-03	0.20	2.00	0.10
H	1E-03	5E-03	2E-02	1E-02	50.0	1E-04	1E-03	0.20	2.00	0.10

(b)

Figure 8

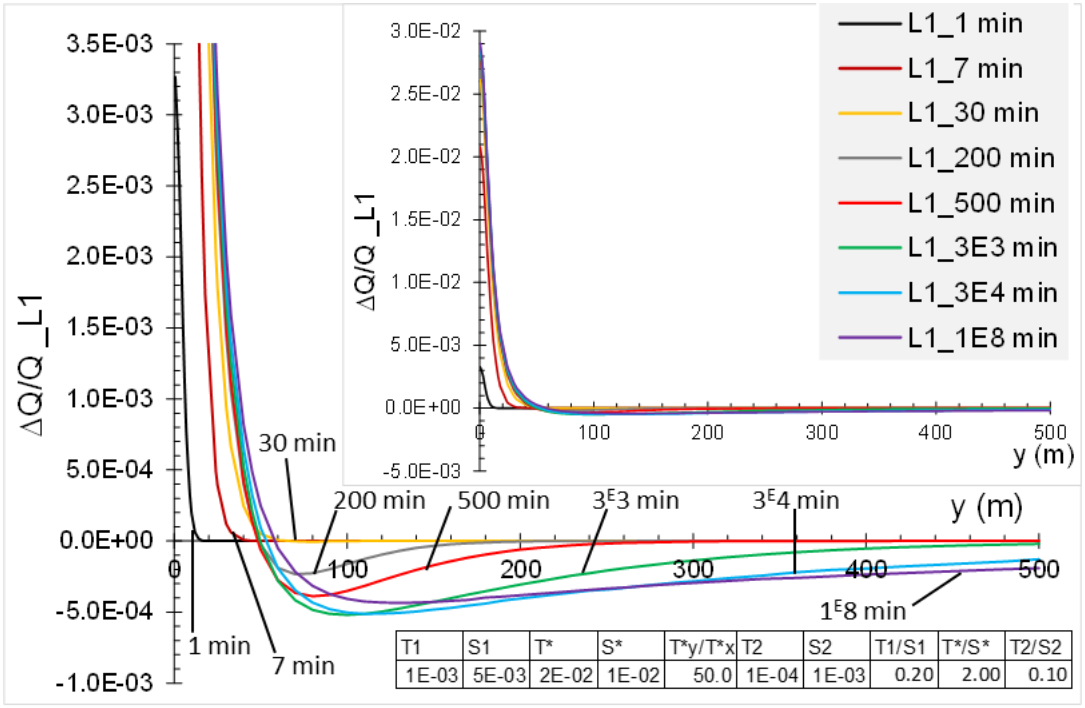

(a)

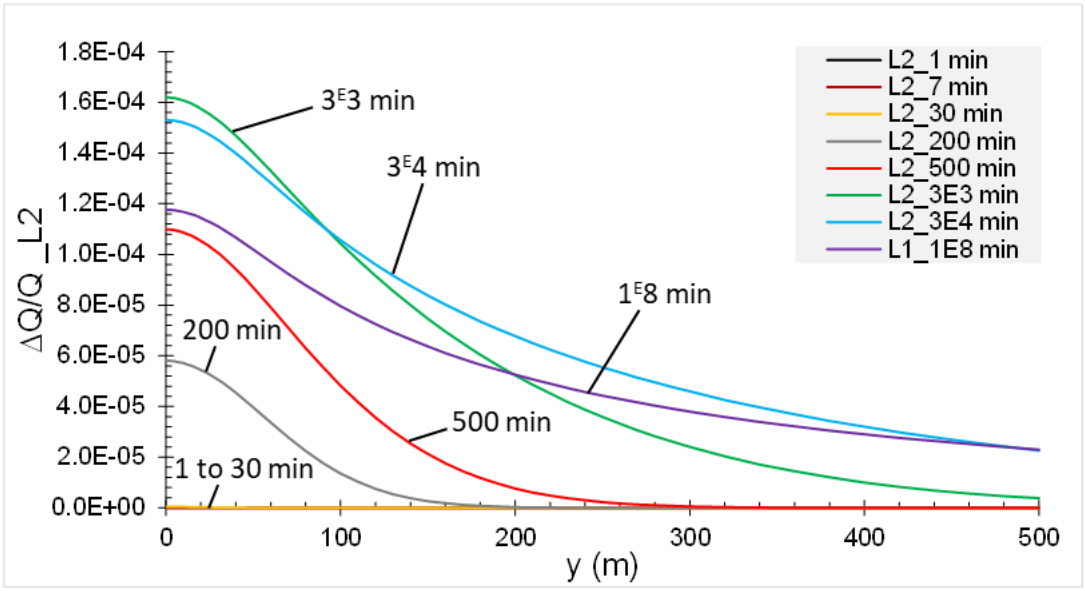

(b)

Figure 9

982

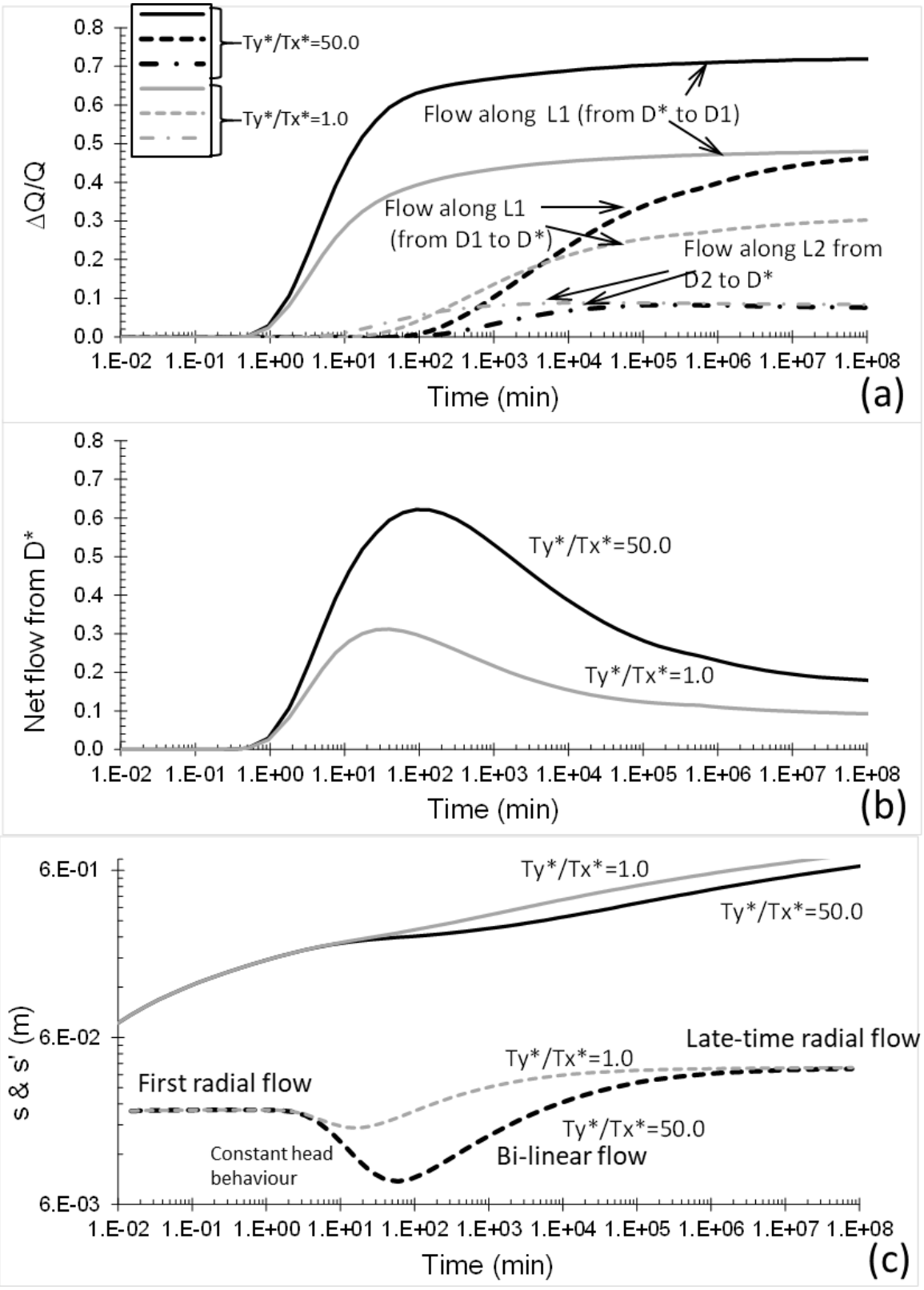

Figure 10

983

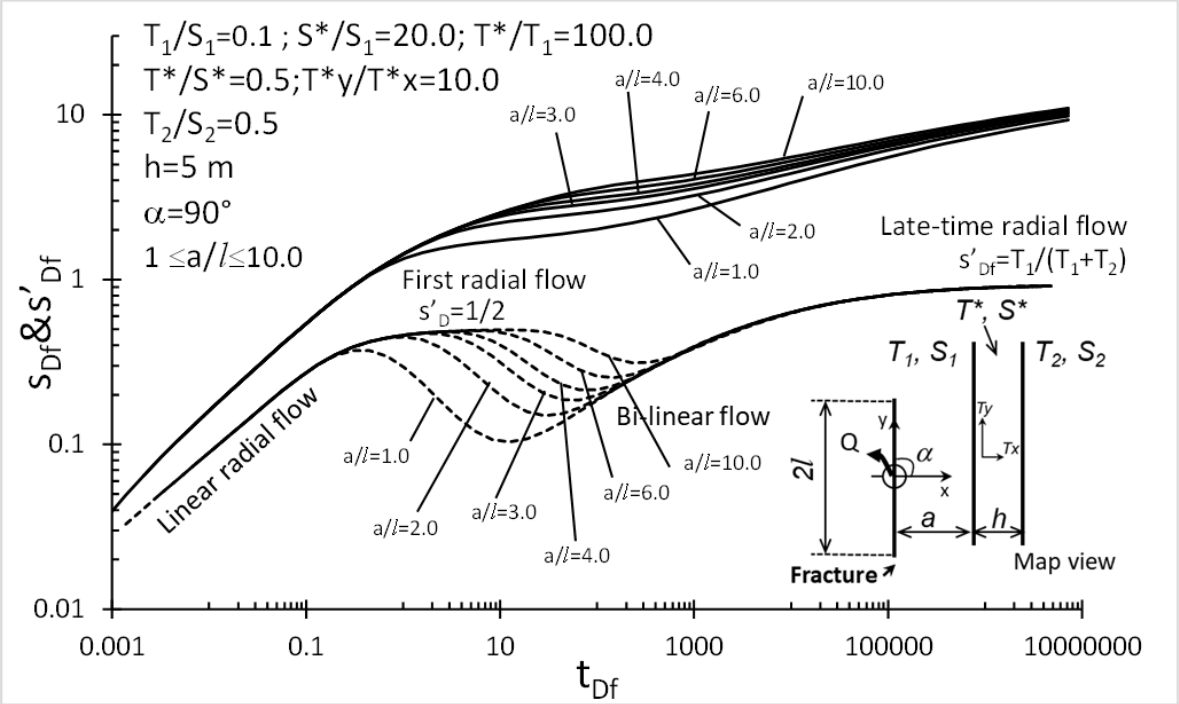

Figure 11

984

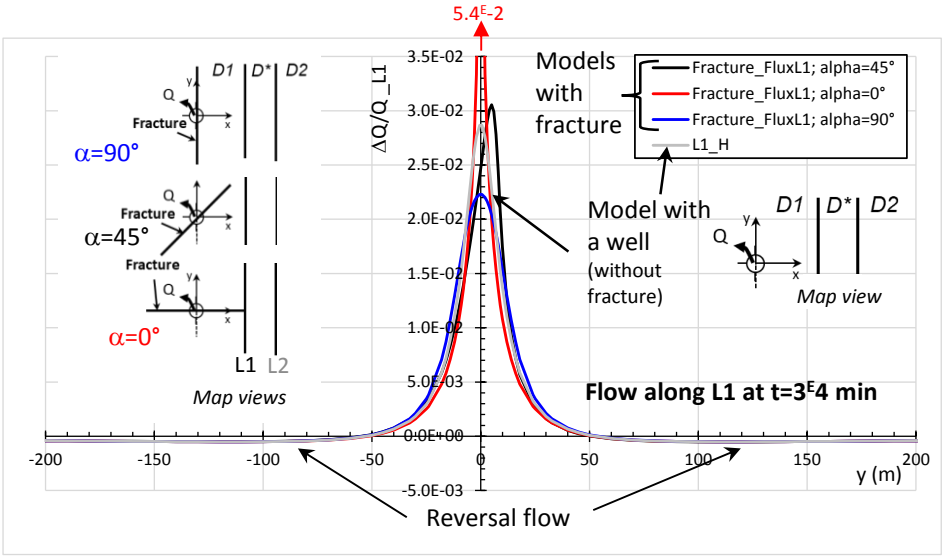

(a)

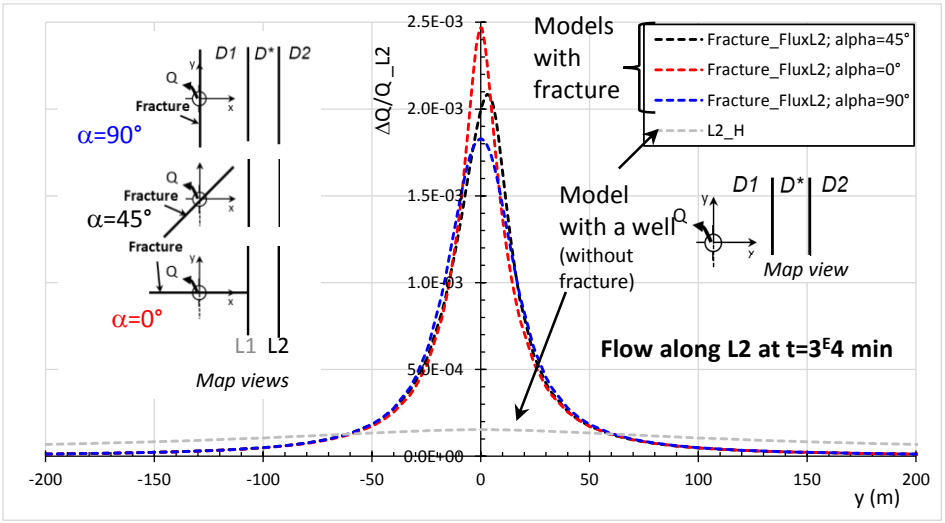

(b)

Figure 12

985

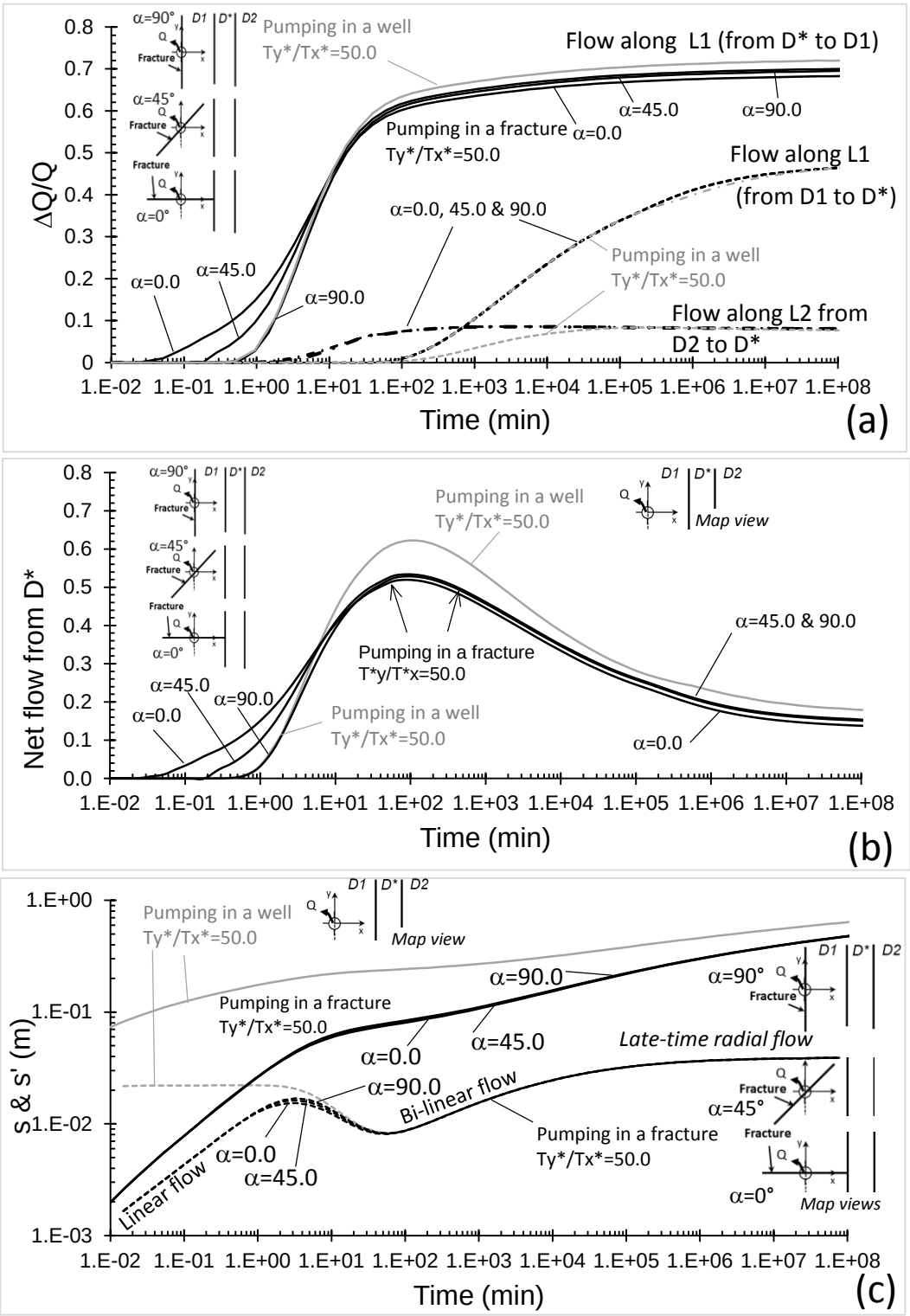
ΔQ/Q
Time (min)
(a)
Pumping in a well
Ty*/Tx*=50.0
Flow along L1 (from D* to D1)
Pumping in a fracture
Ty*/Tx*=50.0
α=0.0
α=45.0
α=90.0
Flow along L1
(from D1 to D*)
α=0.0, 45.0 & 90.0
Flow along L2 from
D2 to D*
Net flow from D*
(b)
Map view
α=45.0 & 90.0
Pumping in a fracture
T*y/T*x=50.0
s & s' (m)
(c)
Late-time radial flow
Bi-linear flow
Linear flow
Map views

Figure 13